$$I(s) = I_a(s) + I_m(s)$$
$$= \frac{I_0}{R^2}\left\{\sum_{i=1}^{M}[|f_i|^2 + |g_i|^2 + 4S_i(s)/(a^2s^4)] + \sum_{i}^{M}\sum_{j\neq i}^{M}[|f_i|\,|f_j|\cos(\eta_i^f - \eta_j^f) + |g_i|\,|g_j|\cos(\eta_i^g - \eta_j^g)] \times \int_0^\infty \mathrm{d}r\, P_{ij}(r,T)(\sin sr)/sr\right\}, \quad (4.3.3.3)$$

where $|g_i|$ and η_i^g refer to the scattering-factor magnitude and phase for electrons that have changed their electron spin state during the scattering process and $|f_i|$ and η_i^f refer to retention of spin orientation. The incident electron beam is assumed to be unpolarized and no attempt has been made to consider relativistic effects on the inelastic scattering cross section, which is usually negligible in the structural s range.

If it is necessary to consider binding effects, the first Born approximation may usually be used in describing molecular scattering, since binding effects are largest for molecules containing small atoms where the Born approximation is most valid.

The exact expression for $I(s)$ in the first Born approximation can be written as (Bonham & Fink, 1974; Tavard & Roux, 1965; Tavard, Rouault & Roux, 1965; Iijima, Bonham & Ando, 1963; Bonham, 1967)

$$I(s) = \frac{4I_0}{a^2s^4R^2}\left\{\sum_{i=1}^{M}(Z_i^2 + Z_i) + \sum_{i}^{M}\sum_{j\neq i}^{M} Z_iZ_j\int_0^\infty \mathrm{d}r\, P_{ij}(r,T)(\sin sr)/sr - 2\sum_{i=1}^{M} Z_i\left\langle\int \mathrm{d}r\,\rho(r+r_i)(\sin sr)/sr\right\rangle_{\mathrm{vib}} + \left\langle\int \mathrm{d}r\,\rho_c(r)(\sin sr)/sr\right\rangle_{\mathrm{vib}}\right\},$$

where

$$\rho(r) = \sum_{i=1}^{N}\int \mathrm{d}r_1 \ldots \int \mathrm{d}r_N\,|\psi(r_1,\ldots,r_N)|^2\delta(r - r_i)$$

and

$$\rho_c(r) = \sum_{i}^{N}\sum_{j\neq i}^{N}\int \mathrm{d}r_1 \ldots \int \mathrm{d}r_N\,|\psi(r_1,\ldots,r_N)|^2\delta(r - r_i + r_j).$$

The brackets $\langle\,\rangle_{\mathrm{vib}}$ denote averaging over the vibrational motion, $\delta(r)$ is the Dirac delta function, and $\psi(r_i,\ldots,r_n)$ is the molecular wavefunction. Binding effects appear to be proportional to the ratio of the number of electrons involved in binding to the total number of electrons in the system (Kohl & Bonham, 1967; Bonham & Iijima, 1965) so that binding effects in molecules containing mainly heavy atoms should be quite small.

The intensities, $I(s)$, for many small molecules have been calculated based on molecular Hartree–Fock wavefunctions. In most cases, a distinctive minimum has been found at about $s = 3 - 4\,\text{Å}^{-1}$ and a much small maximum at $s = 8 - 10\,\text{Å}^{-1}$ in the cross-sectional difference curve between the IAM and the molecular HF results (Pulay, Mawhorter, Kohl & Fink, 1983; Kohl & Bartell, 1969; Liu & Smith, 1977; Epstein & Stewart, 1977; Sasaki, Konaka, Iijima & Kimura, 1982; Shibata, Hirota, Kakuta & Muramatsu, 1980; Horota, Kakuta & Shibata, 1981; Xie, Fink & Kohl, 1984). Further studies using correlated wavefunctions (accounting for up to 60% of the correlation energy) showed that in the elastic channel the binding effects are only weakly modified; only the maximum at $s = 8 - 10\,\text{Å}^{-1}$ is further reduced. However, strong effects are seen in the inelastic channel, deepening the minimum at $s = 3 - 4\,\text{Å}^{-1}$ significantly (Breitenstein, Endesfelder, Meyer, Schweig & Zittlau, 1983; Breitenstein, Endesfelder, Meyer & Schweig, 1984; Breitenstein, Mawhorter, Meyer & Schweig, 1984; Wang, Tripathi & Smith, 1994). Detailed calculations on CO_2 and H_2O averaging over many internuclear distances and applying the pair distribution functions $P_{ij}(r)$ showed that vibrational effects do not alter the binding effects (Breitenstein, Mawhorter, Meyer & Schweig, 1986). For CO_2, the calculations have been confirmed in essence by an experimental set of data (McClelland & Fink, 1985). However, more molecules and more detailed analysis will be available in the future. The binding effects make it desirable to avoid the small-angle-scattering range when structural information is the main goal of a diffraction analysis.

The problem of intramolecular multiple scattering may necessitate corrections to the molecular intensity when three or more closely spaced heavy atoms are present. This correction (Karle & Karle, 1950; Hoerni, 1956; Bunyan, 1963; Gjønnes, 1964; Bonham, 1965*a*, 1966) appears to be more serious for three atoms in a right triangular configuration than for a collinear arrangement of three atoms. A case study by Kohl & Arvedson (1980) on SF_6 showed the importance of multiple scattering. However, their approach is too cumbersome to be used in routine structure work. A very good approximate technique is available utilizing the Glauber approximation (Bartell & Miller, 1980; Bartell & Wong, 1972; Wong & Bartell, 1973; Bartell, 1975); Kohl's results are reproduced quite well using the atomic scattering factors only. Several applications of the multiple scattering routines showed that the internuclear distances are rather insensitive to this perturbation, but the mean amplitudes of vibration can easily change by 10% (Miller & Fink, 1981; Kelley & Fink, 1982*a*; Ketkar & Fink, 1985).

Acknowledgements

The authors acknowledge with gratitude the contributions of Kenneth and Lise Hedberg, who made many helpful suggestions regarding the manuscript and carefully checked the numerical results for smoothness and consistency.

4.3.4. Electron energy-loss spectroscopy on solids (By C. Colliex)

4.3.4.1. *Definitions*

4.3.4.1.1. *Use of electron beams*

Among the different spectroscopies available for investigating the electronic excitation spectrum of solids, inelastic electron scattering experiments are very useful because the range of accessible energy and momentum transfer is very large, as illustrated in Fig. 4.3.4.1 taken from Schnatterly (1979). Absorption measurements with photon beams follow the photon dispersion curve, because it is impossible to vary independently the energy and the momentum of a photon. In a scattering experiment, a quasi-parallel beam of monochromatic particles is incident on the specimen and one measures the changes in energy and momentum that can be attributed to the creation of a given excitation in the target. Inelastic neutron scattering is the most

powerful technique for the low-energy range ($\lesssim 0.1$ eV). On the other hand, inelastic X-ray scattering is well suited for the study of high momentum and large energy transfers because the energy resolution is limited to ~ 1 eV and the cross section increases with momentum transfer. In the intermediate range, inelastic electron scattering [or electron energy-loss spectroscopy (EELS)] is the most useful technique. For recent reviews on different aspects of the subject, the reader may consult the texts by Schnatterly (1979), Raether (1980), Colliex (1984), Egerton (1986), and Spence (1988).

4.3.4.1.2. *Parameters involved in the description of a single inelastic scattering event*

The importance of inelastic scattering as a function of energy and momentum transfer is governed by a double differential cross section:

$$\frac{\mathrm{d}^2\sigma}{\mathrm{d}\Omega\,\mathrm{d}(\Delta E)}, \tag{4.3.4.1}$$

where $\mathrm{d}\Omega$ corresponds to the solid angle of acceptance of the detector and $\mathrm{d}(\Delta E)$ to the energy window transmitted by the spectrometer. The experimental conditions must therefore be defined before any interpretation of the data is possible. Integrations of the cross section over the relevant angular and energy-loss domains correspond to partial or total cross sections, depending on the feature measured. For instance, the total inelastic cross section (σ_i) corresponds to the probability of suffering any energy loss while being scattered into all solid angles. The discrimination between elastic and inelastic signal is generally defined by the energy resolution of the spectrometer, that is the minimum energy loss that can be unambiguously distinguished from the zero-loss peak; it is therefore very dependent on the instrumentation used.

The kinematics of a single inelastic event can be described as shown in Fig. 4.3.4.2. In contrast to the elastic case, there is no simple relation between the scattering angle θ and the transfer of momentum $\hbar\mathbf{q}$. One has also to take into account the energy loss ΔE. Combining both equations of conservation of momentum and energy,

$$\frac{\hbar^2 k'^2}{2m_0} + \Delta E = \frac{\hbar^2 k^2}{2m_0}, \tag{4.3.4.2}$$

and

$$q^2 = k^2 + k'^2 - 2kk'\cos\theta, \tag{4.3.4.3}$$

one obtains

$$(qa_0)^2 = \frac{2E_0}{R}\left[1 - \left(1 - \frac{\Delta E}{E_0}\right)^{1/2}\cos\theta\right] - \frac{\Delta E}{R}, \tag{4.3.4.4}$$

where the fundamental units $a_0 = \hbar^2/m_0e^2 =$ Bohr radius and $R = m_0e^4/2\hbar^2 =$ Rydberg energy are used to introduce dimensionless quantities. In this kinematical description, one deals only with factors concerning the primary or the scattered particle, without considering specifically the information on the ejected electron. For a core-electron excitation of an atom, one distinguishes $\mathbf{q}$ (the momentum exchanged by the incident particle) and $\boldsymbol{\chi}$ (the momentum gained by the excited electron), the difference being absorbed by the recoil of the target nucleus (Maslen & Rossouw, 1983).

4.3.4.1.3. *Problems associated with multiple scattering*

The strong coupling potential between the primary electron and the solid target is responsible for the occurrence of multiple inelastic events (and of mixed inelastic–elastic events) for thick specimens. To describe the interaction of a primary particle with an assembly of randomly distributed scattering centres (with a density N per unit volume), a useful concept is the mean free path defined as

$$\Lambda = 1/N\sigma \tag{4.3.4.5}$$

for the cross section σ. The ratio t/Λ measures the probability of occurrence of the event associated with the cross section σ when the incident particle travels a given length t through the material. This is true in the single scattering case, that is when $t/\Lambda \ll 1$.

For increased thicknesses, one must take into account all multiple scattering events and this contribution begins to be non-negligible for $t \gtrsim$ a few tens of nanometres. Multiple scattering is responsible for a broadening of the angular distribution of the

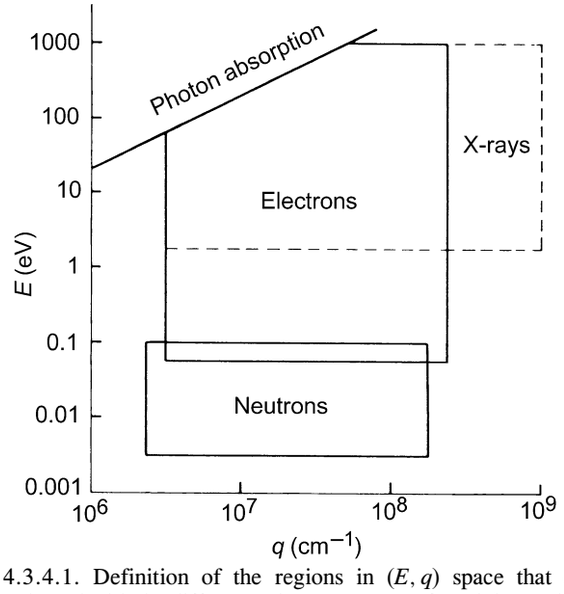

Fig. 4.3.4.1. Definition of the regions in (E, q) space that can be investigated with the different primary sources of particles available at present [courtesy of Schnatterly (1979)].

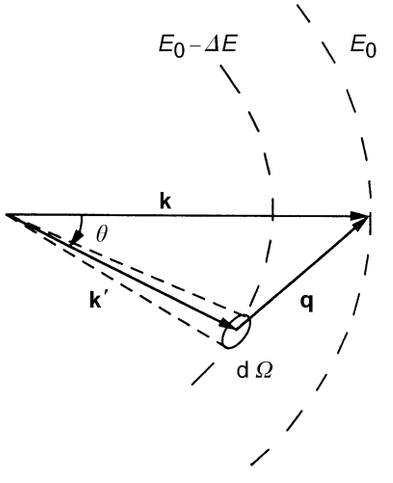

Fig. 4.3.4.2. A primary electron of energy E_0 and wavevector $\mathbf{k}$ is inelastically scattered into a state of energy $E_0 - \Delta E$ and wavevector $\mathbf{k}'$. The energy loss is ΔE and the momentum change is $\hbar\mathbf{q}$. The scattering angle is θ and the scattered electron is collected within an aperture of solid angle $\mathrm{d}\Omega$.

scattering electrons – mostly due to single or multiple elastic events – and of an important fraction of inelastic electrons suffering more than one energy loss. The probability of having n inelastic processes of mean free path Λ is governed by the Poisson distribution:

$$P_n(t) = \frac{1}{n!}\left(\frac{t}{\Lambda}\right)^{-n} \exp\left(-\frac{t}{\Lambda}\right). \qquad (4.3.4.6)$$

Multiple losses introduce additional peaks in the energy-loss spectrum; they are also responsible for an increased background that complicates the detection of single characteristic core-loss signals. Consequently, when the specimen thickness is not very small (*i.e.* for $t \gtrsim 50$ nm for 100 keV primary electrons), it is necessary to retrieve the single scattering profile that is truly representative of the electronic and chemical properties of the specimen.

Deconvolution techniques have therefore been developed to remove the effects of plural scattering from the low-loss spectrum (up to 100 eV) or from ionization edges but very few treatments deal with both angle and energy-loss distributions. Batson & Silcox (1983) have made a detailed study of the inelastic scattering properties of incident 75 keV electrons through a ~100 nm thick polycrystalline aluminium film, over the full range of transferred wavevectors ($0 \rightarrow 3\,\text{Å}^{-1}$) and energy losses ($0 \rightarrow 100$ eV). Schattschneider (1983) has proposed a matrix approach that is sufficiently elaborate to handle angle-resolved energy-loss data. Simpler deconvolution schemes have been proposed and used for processing multiple losses without specific consideration of angular truncation effects. They are valid when the data have been recorded over sufficiently large angles of collection so that all appreciable inelastic scattering is included. They are generally based on Fourier transform techniques, except for the iterative approach of Daniels, Festenberg, Raether & Zeppenfeld (1970), which has been used for energy losses up to about 60 eV (Colliex, Gasgnier & Trebbia, 1976). The most accurate current methods are the Fourier-log method of Johnson & Spence (1974) and Spence (1979), and the Fourier-ratio method of Swyt & Leapman (1982), which only applies to the core-loss region. The first is far more complete and accurate and applies to any spectral range when one has recorded a full spectrum in unsaturated conditions.

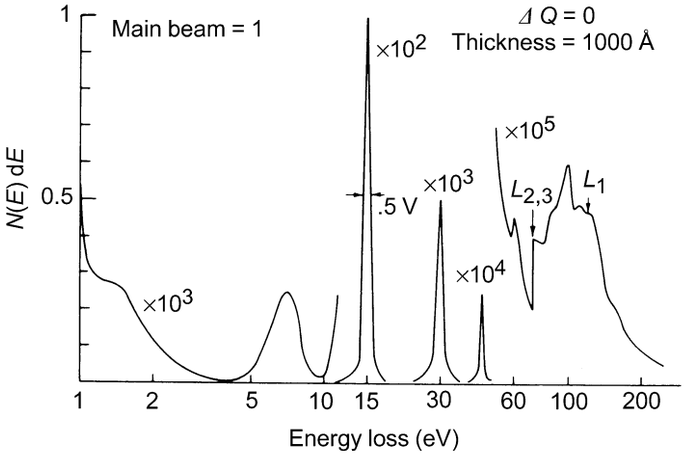

Fig. 4.3.4.3. Excitation spectrum of aluminium from 1 to 250 eV, investigated by EELS on 300 keV primary electrons [courtesy of Schnatterly (1979)].

4.3.4.1.4. *Classification of the different types of excitations contained in an electron energy-loss spectrum*

Figs. 4.3.4.3 and 4.3.4.4 display examples of electron energy-loss spectra over large energy domains, typically from 1 to about 2000 eV. With one instrument, all elementary excitations from the near infrared to the X-ray domain can be investigated. Apart from the main beam or zero-loss peak, two major families of electronic transitions can be distinguished in such spectra:

(*a*) The excitations in the low or moderate energy-loss region ($1 < \Delta E < 50$ eV) concern the quasifree (valence and conduction) electron gas. In a pure metal, such as Al, the dominant feature is the intense narrow peak at 15 eV with its multiple satellites at about 30, 45, and 60 eV. One also detects an interband transition at 1.5 eV and a surface plasmon peak at ~ 7 eV. For the more complex mineral specimen, rhodizite, this contribution lies in the intense and broad, but not very specific, peak around 25 eV. All these features are discussed in detail in Subsection 4.3.4.3.

(*b*) The excitations in the high-energy-loss domain ($50 < \Delta E < 2000$ eV) concern excitation and ionization processes from core atomic orbitals: in Al, the $L_{2,3}$ edge is associated with the creation of holes on the $2p$ level, L_1 is due to the excitation of $2s$, and K of $1s$ electrons. These contributions appear as edges superposed on a regularly decreasing background. In the complex specimen, the succession of these

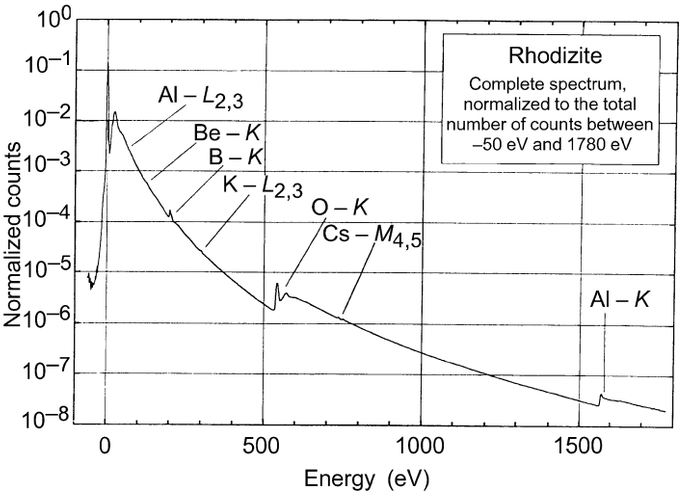

Fig. 4.3.4.4. Complete electron energy-loss spectrum of a thin rhodizite crystal (thickness ~60 nm). Separate spectra from eight significantly overlapping energy ranges were measured and matched. Primary energy 60 keV. Semi-angle of collection 5 mrad. Recording time 300 s (parallel acquisition). Scanned area 30×40 nm. Analysed mass 2×10^{-15} g [courtesy of Engel, Sauer, Zeitler, Brydson, Williams & Thomas (1988)].

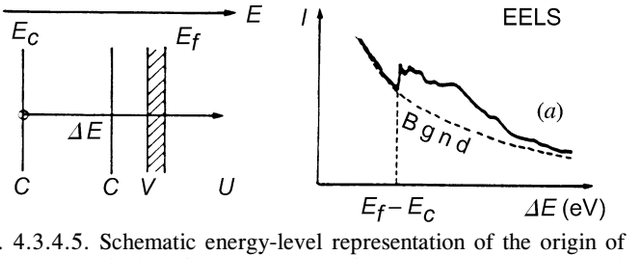

Fig. 4.3.4.5. Schematic energy-level representation of the origin of a core-loss excitation (from a core level C at energy E_c to an unoccupied state U above the Fermi level E_f) and its general shape in EELS, as superimposed on a continuously decreasing background.

different edges on top of the monotonously decaying background is a signature of the elemental composition, the intensity of the signals being roughly proportional to the relative concentration in the associated element. Core-level EELS spectroscopy therefore investigates transitions from one well defined atomic orbital to a vacant state above the Fermi level: it is a probe of the energy distribution of vacant states in a solid, see Fig. 4.3.4.5. As the excited electron is promoted on a given atomic site, the information involved has two specific characters: it provides the local atomic point of view and it reflects the existence of the hole created, which can be more or less screened by the surrounding population of electrons in the solid. The properties of this family of excitations are the subject of Subsection 4.3.4.4.

The non-characteristic background is due to the superposition of several contributions: the high-energy tail of valence-electron scattering, the tails of core losses with lower binding energy, *Bremsstrahlung* energy losses, plural scattering, *etc*. It is therefore rather difficult to model its behaviour, although some efforts have been made along this direction using Monte Carlo simulation of multiple scattering (Jouffrey, Sevely, Zanchi & Kihn, 1985).

When one monochromatizes the natural energy width of the primary beam to much smaller values (about a few meV) than its natural width, one has access to the infrared part of the electromagnetic spectrum. An example is provided in Fig. 4.3.4.6 for a specimen of germanium in the energy-loss range 0 up to 500 meV. In this case, one can investigate phonon modes, or the bonding states of impurities on surfaces. This field has been much less extensively studied than the higher-energy-loss range [for references see Ibach & Mills (1982)].

Generally, EELS techniques can be applied to a large variety of specimens. However, for the following review to remain of limited size, it is restricted to electron energy-loss spectroscopy on solids and surfaces in transmission and reflection. It omits some important aspects such as electron energy-loss spectroscopy in gases with its associated information on atomic and molecular states. In this domain, a bibliography of inner-shell excitation studies of atoms and molecules by electrons, photons or theory is available from Hitchcock (1982).

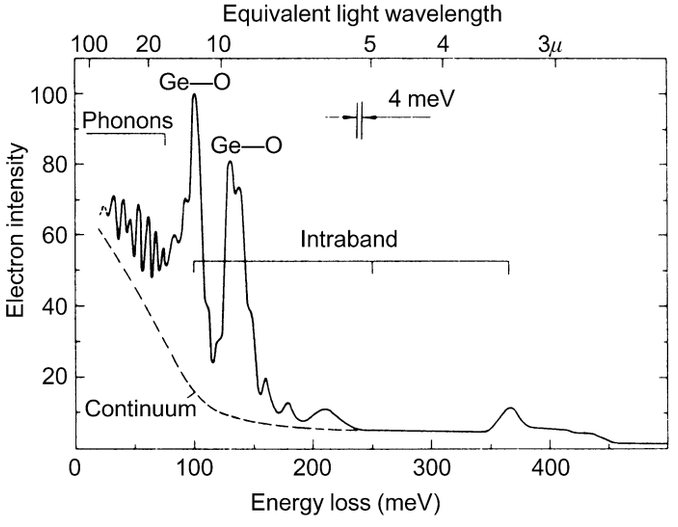

Fig. 4.3.4.6. Energy-loss spectrum, in the meV region, of an evaporated germanium film (thickness $\simeq 25$ nm). Primary electron energy 25 keV. Scattering angle $< 10^{-4}$. One detects the contributions of the phonon excitation, of the Ge—O bonding, and of intraband transitions [courtesy of Schröder & Geiger (1972)].

Table 4.3.4.1. *Different possibilities for using EELS information as a function of the different accessible parameters* ($\mathbf{r}$, θ, ΔE)

	Integration parameter	Selection parameter	Results	Working mode of the spectrometer
1	$\boldsymbol{\theta}$	$\mathbf{r}$	Spectrum $I_{\mathbf{r}}$ (ΔE)	Analyser
2	$\mathbf{r}$	$\boldsymbol{\theta}$	Spectrum $I_{\boldsymbol{\theta}}$ (ΔE)	Analyser
3	$\boldsymbol{\theta}$	ΔE	Energy-filtered image $I_{\Delta E}(\mathbf{r})$	Filter
4	$\mathbf{r}$	ΔE	Energy-filtered diffraction pattern $I_{\Delta E}(\boldsymbol{\theta})$	Filter

4.3.4.2. *Instrumentation*

4.3.4.2.1. *General instrumental considerations*

In a dedicated instrument for electron inelastic scattering studies, one aims at the best momentum and energy resolution with a well collimated and monochromatized primary beam. This is achieved at the cost of poor spatial localization of the incident electrons and one assumes the specimens to be homogeneous over the whole irradiated volume. In a sophisticated instrument such as that built by Fink & Kisker (1980), the energy resolution can be varied from 0.08 to 0.7 eV, and the momentum transfer resolution between 0.03 and 0.2 Å^{-1}, but typical values for the electron-beam diameter are about 0.2 to 1 mm. Nowadays, many energy-analysing devices are coupled with an electron microscope: consequently, an inelastic scattering study involves recording for a primary intensity I_0, the current $I(\mathbf{r}, \boldsymbol{\theta}, \Delta E)$ scattered or transmitted at the position $\mathbf{r}$ on the specimen, in the direction $\boldsymbol{\theta}$ with respect to the primary beam, and with an energy loss ΔE. Spatial resolution is achieved either with a focused probe or by a selected area method, angular acceptance is defined by an aperture, and energy width is controlled by a detector function after the spectrometer. It is not possible from signal-to-noise considerations to reduce simultaneously all instrumental widths to very small values. One of the parameters ($\mathbf{r}$, $\boldsymbol{\theta}$ or ΔE) is chosen for signal integration, another for selection, and the last is the variable. Table 4.3.4.1. classifies these different possibilities for inelastic scattering studies.

Because of the great variety of possible EELS experiments, it is impossible to build an optimum spectrometer for all applications. For instance, the design of a spectrometer for low-energy incident electrons and surface studies is different from that for high-energy incident electrons and transmission work. In the latter category, instruments built for dedicated EELS studies (Killat, 1974; Gibbons, Ritsko & Schnatterly, 1975; Fink & Kisker, 1980; *etc*.) are different from those inserted within an electron-microscope environment, in which case it is possible to investigate the excitation spectrum from a specimen area well characterized in image and diffraction [see the reviews by Colliex (1984) and Egerton (1986)].

The literature on dispersive electron–optical systems (equivalent to optical prisms) is very large. For example, the theory of uniform field magnets, which constitute an important family of analysing devices, has been extensively developed for the components in high-energy particle accelerators (Enge, 1967; Livingood, 1969). As for EELS spectrometers, they can be classified as:

(*a*) *Monochromators*, which filter the incident beam to obtain the smallest primary energy width. The natural width for a heated W filament is about 1 eV, possibly rising to about a few eV as a consequence of stochastic interactions [Boersch (1954) effect, analysed for instance by Rose & Spehr (1980)]. For a low-temperature field-emission source, this energy spread is only ~0.3 eV. This constitutes a clear gain but remains insufficient for meV studies. In this case, one has to introduce a filter lens such as the three-electrode design developed by Hartl (1966) or a cylindrical electrostatic deflector before the accelerator [Kuyatt & Simpson (1967) or Gibbons *et al.* (1975)]. In both cases, an energy resolution of 50 meV has been achieved for electron beams of 50–300 keV at the specimen.

(*b*) *Analysers*, which measure the energy distribution of the beam scattered from the specimen. They can be used either strictly as analysers displaying the energy loss from a given specimen volume, or as filters (or selecting devices) that provide 2D images or diffraction patterns with a given energy loss.

4.3.4.2.2. *Spectrometers*

Fig. 4.3.4.7 defines the basic parameters of a 'general' energy-loss spectrometer: a region of electrostatic **E** and/or magnetic **B** fields transforms a distribution of electrons I_0 $(x_0, y_0, t_0, u_0, \rho)$ in the object plane of coordinate z_0 along the principal trajectory, into a distribution of electrons I_1 $(x_1, y_1, t_1, u_1, \rho)$ in the object plane of coordinate z_1, coincident with the detector plane (or optically conjugate to it). The transverse coordinates are labelled as (x, y), the angular ones as (t, u), and $\rho = \Delta p/p = \Delta E/2E$ is the relative change in absolute momentum value associated with the energy loss.

Common properties of such systems are:

(*a*) first-order imaging properties or stigmatism, *i.e.* all electrons leaving (x_0, y_0) are focused at the same (x_1, y_1) point, independently of their inclination on the optical axis;

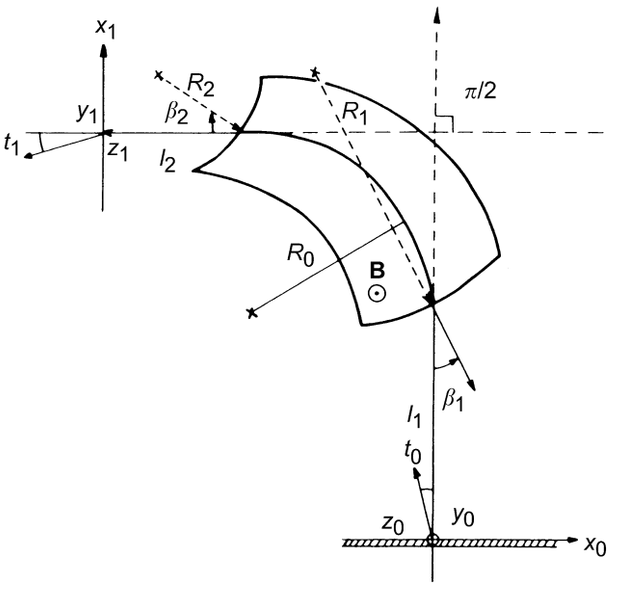

Fig. 4.3.4.7. Schematic drawing of a uniform magnetic sector spectrometer with induction **B** normal to the plane of the figure. Definition of the coordinates used in the text (the object plane at coordinate z_0 along the mean trajectory coincides with the specimen, and the image plane at z_1 coincides with the dispersion plane and the detector level).

(*b*) strong chromatic aberration in order to realize an efficient discrimination between electrons of different ρ.

The spectrometer performance can be evaluated with the following parameters:

$D = dispersion =$ beam displacement in the spectrometer image plane for a given momentum change ρ; it is generally expressed in cm/eV. The higher the dispersion, the easier it is to resolve small energy losses. For a straight-edge 90° magnetic sector, $D \propto 2R/E_0$, where R is the curvature radius of the mean trajectory and E_0 is the primary energy.

$\delta E_{\min} = energy\ resolution$. This corresponds to the minimum-energy variation that can be resolved by the instrument. It takes into account the width of the image $\Delta x_{\text{image}} = Mr$, where M is the spectrometer magnification and r the radius of the spectrometer source, as well as the second- and higher-order angular aberrations. These are responsible for the imperfect focusing of the electrons that enter the spectrometer within a cone of angular acceptance β_0 and contribute through a term $\Delta x_{\text{aber}} = C\beta_0^2$. Moreover, one must convolute these terms with the natural width δE_0 of the primary beam, including AC fields, and with the detection slit width Δx_{slit}. Combining all these effects, as shown schematically in Fig. 4.3.4.8, one obtains approximately:

$$\Delta x_{\text{tot}} = [(\Delta x_{\text{slit}})^2 + (\Delta x_{\text{image}})^2 + (\Delta x_{\text{aber}})^2 + D\delta E_0^2]^{1/2} \quad (4.3.4.7)$$

and the corresponding energy resolution is defined as $\delta E_{\min} = (\Delta x_{\text{tot}})_{\min}/D$. In many situations, the dominant factor is the second-order aberration term $C\beta_0^2$ so that the figure of merit F, defined as $F = \pi\beta_0 E_0/\delta E_{\min}$, is of the order of unity for an uncorrected magnetic spectrometer.

From this simplified discussion, one deduces that there is generally competition between large angular acceptance for the inelastic signal, which is very important for obtaining a high signal-to-noise ratio (SNR) for core-level excitations, and good energy resolution. Two solutions have been used to remedy this limitation. The first is to improve spectrometer design, for example by correcting second-order aberrations in a homogeneous magnetic prism (Crewe, 1977*a*; Parker, Utlaut & Isaacson, 1978; Egerton, 1980*b*; Krivanek & Swann, 1981; *etc*). This can enhance the figure of merit by at least a factor of 100. The second possibility is to transform the distribution of electrons to be analysed at the exit surface of the specimen into a more convenient distribution at the spectrometer entrance. This can be done by introducing versatile transfer optics (see Crewe, 1977*b*; Egerton, 1980*a*; Johnson, 1980; Craven & Buggy, 1981; *etc*.). As a final remark on the energy resolution of a spectrometer, it is meaningless to define it without reference to the size and the angular aperture of the analysed beam.

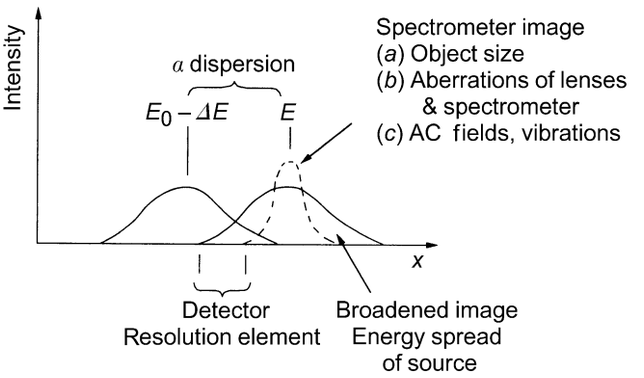

Fig. 4.3.4.8. Different factors contributing to the energy resolution in the dispersion plane [courtesy of Johnson (1979)].

Historically, many types of spectrometer have been used since the first suggestion by Wien (1897) that an energy analyser could be designed by employing crossed electric and magnetic fields. Reviews have been published by Klemperer (1965), Metherell (1971), Pearce-Percy (1978), and Egerton (1986). Nowadays, two configurations are mostly used and have become commercially available on modern electron microscopes: these are spectrometers on TEM/STEM instruments and filters on CTEM ones. In the first case, *homogeneous magnetic sectors* are the simplest and most widely used devices. Recent instrumental developments by Shuman (1980), Krivanek & Swann (1981), and Scheinfein & Isaacson (1984) have given birth to a generation of spectrometers with the following major characteristics: double focusing, correction for second-order aberrations, dispersion plane perpendicular to the trajectory. This has been made possible by a suitable choice of several parameters, such as the tilt angles and the radius of curvature for the entrance and exit faces and the correct choice of the object source position. As an example, for a 100 keV STEM equipped with a field emission gun, the coupling illustrated in Fig. 4.3.4.9 leads to an energy resolution of 0.35 eV for $\beta_0 = 7.5$ mrad on the specimen as visible on the elastic peak, and 0.6 eV for $\alpha_0 = 25$ mrad as checked on the fine structures on core losses. Krivanek, Manoubi & Colliex (1985) demonstrated a sub-eV energy resolution over the whole range of energy losses up to 1 or 2 keV.

A very competitive solution is the *Wien filter*, which consists of uniform electric and magnetic fields crossed perpendicularly, see Fig. 4.3.4.10. An electron travelling along the axis with a velocity $\mathbf{v}_0$ such that $|\mathbf{v}_0| = E/B$ is not deflected, the net force on it being null. All electrons with different velocities, or at some angle with respect to the optical axis, are deflected. The dispersion of the system is greatly enhanced by decelerating the electrons to about 100 eV within the filter, in which case $D \simeq$ a few 100 μm/eV. A presently achievable energy resolution of 150 meV at a spectrometer collection half-angle of 12.5 mrad has been demonstrated by Batson (1986, 1989). It allows the study of the detailed shape of the energy distribution of the electrons emitted from a field emission source and the taking of it into account in the investigation of band-gap states in semiconductors (Batson, 1987).

Filtering devices have been designed to form an energy-filtered image or diffraction pattern in a CTEM. The first

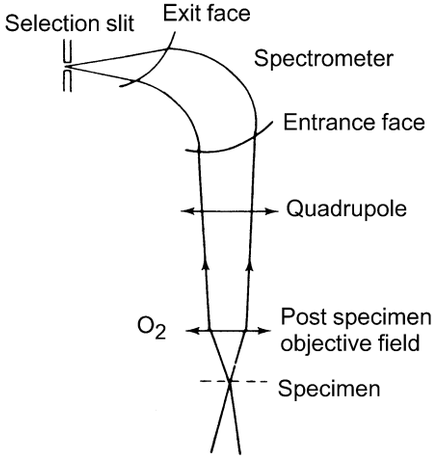

Fig. 4.3.4.9. Optical coupling of a magnetic sector spectrometer on a STEM column.

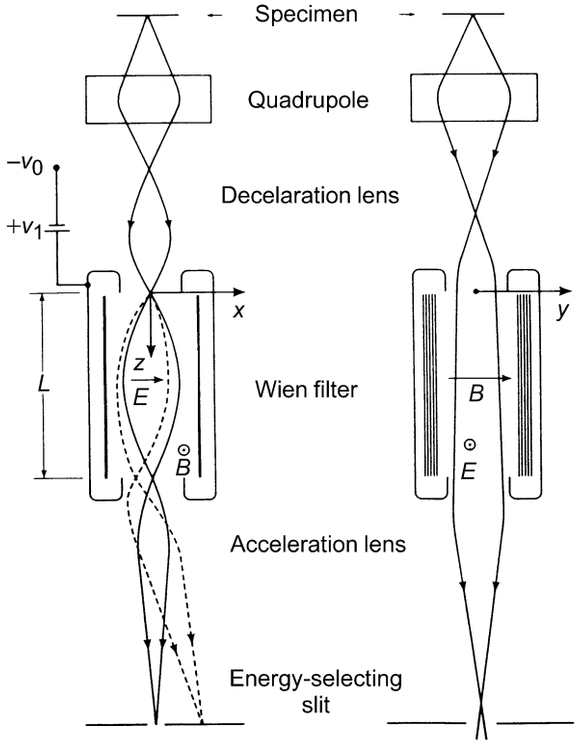

Fig. 4.3.4.10. Principle of the Wien filter used as an EELS spectrometer: the trajectories are shown in the two principal (dispersive and focusing) sections.

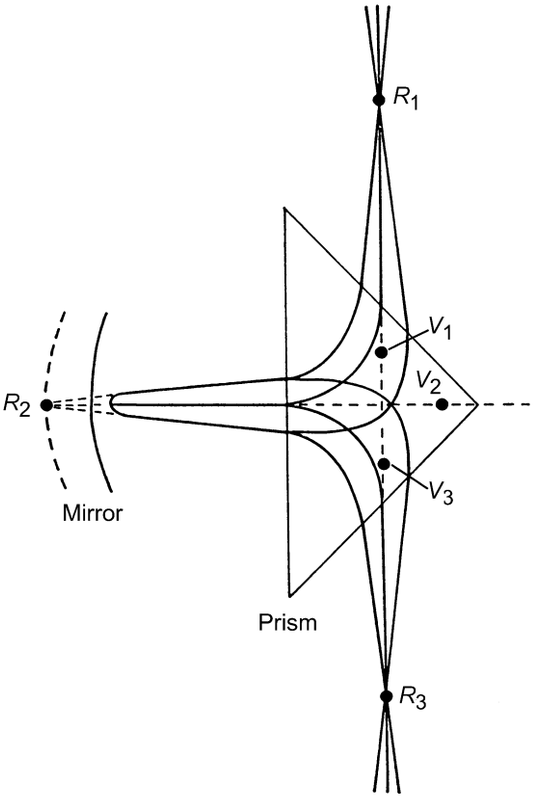

Fig. 4.3.4.11. Principle of the Castaing & Henry filter made from a magnetic prism and an electrostatic mirror. (R_1, R_2, and R_3 are the real conjugate stigmatic points, and V_1, V_2, and V_3 the virtual ones: the dispersion plane coincides with the R_3 level and achromatic one with the V_3 level.)

Table 4.3.4.2. *Plasmon energies measured (and calculated) for a few simple metals; most data have been extracted from Raether (1980)*

Monovalent			Divalent			Trivalent			Tetravalent		
$\hbar\omega_p$ (eV)			$\hbar\omega_p$ (eV)			$\hbar\omega_p$ (eV)			$\hbar\omega_p$ (eV)		
	Meas.	Calc.		Meas.	Calc.		Meas.	Calc.		Meas.	Calc.
Li	7.1	(8.0)	Be	18.7	(18.4)	B	22.7	(?)	C	34.0	(31)
Na	5.7	(5.9)	Mg	10.4	(10.9)	Al	14.95	(15.8)	Si	16.5	(16.6)
K	3.7	(4.3)	Ca	8.8	(8.0)	Ga	13.8	(14.5)	Ge	16.0	(15.6)
Rb	3.4	(3.9)	Sr	8.0	(7.0)	In	11.4	(12.5)	Sn	13.7	(14.3)
Cs	2.9	(3.4)	Ba	7.2	(6.7)	Sc	14.0	(12.9)	Pb	(13)	(13.5)

solution, reproduced in Fig. 4.3.4.11, is due to Castaing & Henry (1962). It consists of a double magnetic prism and a concave electrostatic mirror biased at the potential of the microscope cathode. The system possesses two pairs of stigmatic points that may coincide with a diffraction plane and an image plane of the electron-microscope column. One of these sets of points is achromatic and can be used for image filtering. The other is strongly chromatic and is used for spectrum analysis. Zanchi, Sevely & Jouffrey (1977) and Rose & Plies (1974) have proposed replacing this system, which requires an extra source of high voltage for the mirror, by a purely magnetic equivalent device. Several solutions, known as the α and ω filters, with three or four magnets, have thus been built, both on very high voltage microscopes (Zanchi, Perez & Sevely, 1975) and on more conventional ones (Krahl & Herrmann, 1980), the latest version now being available from one EM manufacturer (Zeiss EM S12).

4.3.4.2.3. *Detection systems*

The final important component in EELS is the detector that measures the electron flux in the dispersion plane of the spectrometer and transfers it through a suitable interface to the data storage device for further computer processing. Until about 1990, all systems were operated in a sequential acquisition mode. The dispersed beam was scanned in front of a narrow slit located in the spectrometer dispersion plane. Electrons were then generally recorded by a combination of scintillator and photomultiplier capable of single electron counting.

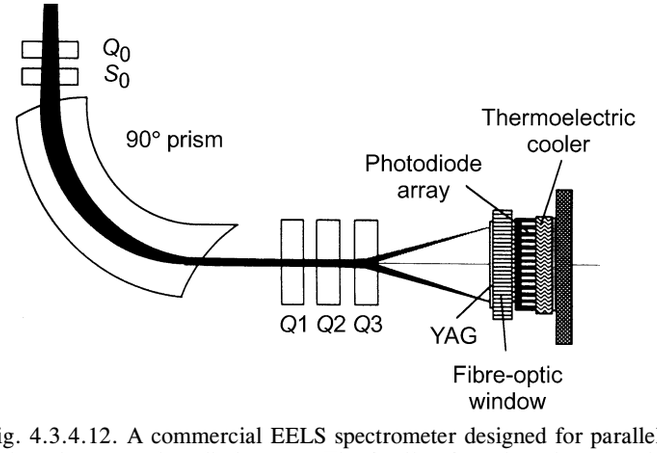

Fig. 4.3.4.12. A commercial EELS spectrometer designed for parallel detection on a photodiode array. The family of quadrupoles controls the dispersion on the detector level [courtesy of Krivanek *et al.* (1987))].

This process is, however, highly inefficient: while the counts are measured in one channel, all information concerning the other channels is lost. These requirements for improved detection efficiency have led to the consideration of possible solutions for parallel detection of the EELS spectrum. They use a multiarray of detectors, the position, the size and the number of which have to be adapted to the spectral distribution delivered by the spectrometer. In most cases with magnetic type devices, auxiliary electron optics has to be introduced between the spectrometer and the detector so that the dispersion matches the size of the individual detection cells. Different systems have been proposed and tested for recording media, the most widely used solutions at present being the photodiode and the charge-coupled diode arrays described by Shuman & Kruit (1985), Krivanek, Ahn & Keeney (1987), Strauss, Naday, Sherman & Zaluzec (1987), Egerton & Crozier (1987), Berger & McMullan (1989), *etc.* Fig. 4.3.4.12 shows a device, now commercially available from Gatan, that is made of a convenient combination of these different components. This progress in detection has led to significant improvements in many areas of EELS: enhanced detection limits, reduced beam damage in sensitive materials, data of improved quality in terms of both SNR and resolution, and access to time-resolved spectroscopy at the ms time scale (chronospectra). Several of these important consequences are illustrated in the following sections.

4.3.4.3. *Excitation spectrum of valence electrons*

Most inelastic interaction of fast incident electrons is with outer atomic shells in atoms, or in solids with valence electrons (referred to as conduction electrons in metals). These involve excitations in the 0–50 eV range, but, in a few cases, interband transitions from low-binding-energy shells may also contribute.

4.3.4.3.1. *Volume plasmons*

The basic concept introduced by the many-body theory in the interacting free electron gas is the volume plasmon. In a condensed material, the assembly of loosely bound electrons behaves as a plasma in which collective oscillations can be induced by a fast external charged particle. These eigenmodes, known as *volume plasmons*, are longitudinal charge-density fluctuations around the average bulk density in the plasma $n \simeq 10^{28}$ e$^-$/m^3). Their eigen frequency is given, in the free electron gas, as

$$\omega_p = \left(\frac{n e^2}{m\varepsilon_0}\right)^{1/2}. \qquad (4.3.4.8)$$

The corresponding $\hbar\omega_p$ energy, measured in an energy-loss spectrum (see the famous example of the plasmon in aluminium

Table 4.3.4.3. *Experimental and theoretical values for the coefficient α in the plasmon dispersion curve together with estimates of the cut-off wavevector (from Raether, 1980)*

	Measured α	Calculated α	q_c (Å^{-1})
Li	0.24	0.35	0.9
Na	0.24	0.32	0.8
K	0.14	0.29	0.8
Mg	0.35	0.39	1.0
Al	0.2 (<0.5 Å^{-1})		
	0.45 (>0.5 Å^{-1})	0.43	1.3
In	0.40 (<0.5 Å^{-1})		
	0.66 (>0.5 Å^{-1})		
Si	0.41		
	0.3	0.45	1.1

Table 4.3.4.4. *Comparison of measured and calculated values for the halfwidth $\Delta E_{1/2}(0)$ of the plasmon line (from Raether, 1980)*

	Experimental (eV)	Theory (eV)
Li	2.2	2.55
Na	0.3	0.12
K	0.25	0.15
Rb	0.6	0.64
Cs	1.2	0.96
Al	0.53	0.43
Mg	0.7	0.7
Si	3.2	5.4
Ge	3.1	3.9

in Fig. 4.3.4.3), is the *plasmon energy*, for which typical values in a selection of pure solid elements are gathered in Table 4.3.4.2. The accuracies of the measured values depend on several instrumental parameters. Moreover, they are sensitive to the specimen crystalline state and to its degree of purity. Consequently, there exist slight discrepancies between published values. Numbers listed in Table 4.3.4.2 must therefore be accepted with a 0.1 eV confidence. Some specific cases require comments: amorphous boron, when prepared by vacuum evaporation, is not a well defined specimen. Carbon exists in several allotropic varieties. The selection of the diamond type in the table is made for direct comparison with the other tetravalent specimens (Si, Ge, Sn). The results for lead (Pb) are still subject to confirmation. The volumic mass density is an important factor (through n) in governing the value of the plasmon energy. It varies with temperature and may be different in the crystal, in the amorphous, and in the liquid phases. In simple metals, the amorphous state is generally less dense than the crystalline one, so that its plasmon energy shifts to lower energies.

The above description applies only to very small scattering vectors $\mathbf{q}$. In fact, the plasmon energy increases with scattering angle (and with momentum transfer $\hbar\mathbf{q}$). This dependence is known as the dispersion relation, in which two distinct behaviours can be described:

(a) For small momentum transfers ($q \lesssim q_c$), the dispersion curve is parabolic:

$$\hbar\omega_p(q) = \hbar\omega_p(0) + \frac{\alpha\hbar^2}{m_0} q^2. \qquad (4.3.4.9)$$

The coefficient α has been measured in a number of substances and calculated for the free-electron case in the random phase approximation (Lindhard, 1954); see Table 4.3.4.3 for some data. A simple expression for α is

$$\alpha = \tfrac{3}{5}\frac{E_F}{\hbar\omega_p(0)}, \qquad (4.3.4.10)$$

where E_F is the Fermi energy of the electron gas. More detailed observations indicated that it is not possible to describe the dispersion curve over a large momentum range with a single q^2 law. In fact, one has to fit the experiment data with different linear or quadratic slopes as a function of q [see values indicated for Al and In in Table 4.3.4.3, and Hohberger, Otto & Petri (1975)]. Moreover, anisotropy has been found along different $\mathbf{q}$ directions in monocrystals (Manzke, 1980). In parallel, refinements have been brought into the calculations by including band-structure effects to deal with the anisotropy of the dispersion relation and with the bending of the experimental curves. Electron–electron correlations have also been considered, which has slightly improved the agreement between calculated and measured values of α (Bross, 1978*a*, *b*).

(b) For large momentum transfers, there exists a critical wavevector q_c, which corresponds to a strong decay of the plasmon mode into single electron–hole pair excitations. This can be calculated using conservation rules in energy and momentum, giving

$$\hbar\omega_p(0) + \alpha\frac{\hbar^2}{m_0} q_c^2 = \frac{\hbar^2}{2m_0}(q_c^2 + 2q_c q_F), \qquad (4.3.4.11)$$

where q_F is the Fermi wavevector. A simple approximation is $q_c \simeq \omega_p/v_F$, v_F being the Fermi velocity. Single pair excitations can be created by fast incoming electrons in the domain of scattering conditions contained between the two curves:

$$\left.\begin{aligned} \Delta E_{\max} &= \frac{\hbar^2}{2m_0}(q^2 + 2qq_F) \\ \Delta E_{\min} &= \frac{\hbar^2}{2m_0}(q^2 - 2qq_F) \end{aligned}\right\} \qquad (4.3.4.12)$$

shown in Fig. 4.3.4.13. They bracket the curve $\Delta E = \hbar^2 q^2/2m_0$ corresponding to the transfer of energy and momentum to an isolated free electron. For momentum transfers such as $q > q_c$, the plasmon mode is heavily damped and it is difficult to distinguish its own specific behaviour from the electron–hole continuum. A few studies, *e.g.* Batson & Silcox (1983), indicate that the plasmon dispersion curve flattens as it enters the

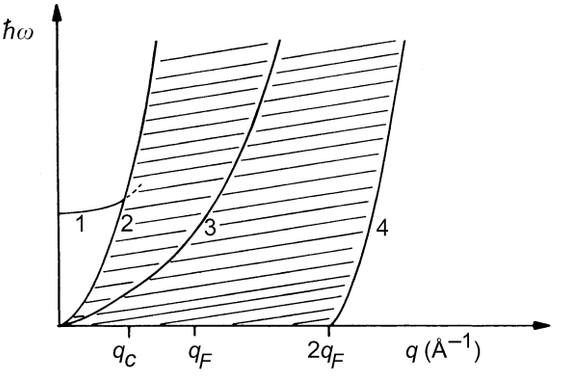

Fig. 4.3.4.13. The dispersion curve for the excitation of a plasmon (curve 1) merges into the continuum of individual electron–hole excitations (between curves 2 and 4) for a critical wavevector q_c. The intermediate curve (3) corresponds to Compton scattering on a free electron.

quasiparticle domain and approaches the centre of the continuum close to the free-electron curve. However, not only is the scatter between measurements fairly high, but a satisfactory theory is not yet available [see Schattschneider (1989) for a compilation of data on the subject].

Plasmon lifetime is inversely proportional to the energy width of the plasmon peak $\Delta E_{1/2}$. Even for Al, with one of the smallest plasmon energy widths ($\simeq 0.5$ eV), the lifetime is very short: after about five oscillations, their amplitude is reduced to $1/e$. Such a damping demonstrates the strength of the coupling of the collective modes with other processes. Several mechanisms compete for plasmon decay:

(*a*) For small momentum transfer, it is generally attributed to vertical interband transitions. Table 4.3.4.4, extracted from Raether (1980), compares a few measured values of $\Delta E_{1/2}(0)$, with values calculated using band-structure descriptions.

(*b*) For moderate momentum transfer q, a variation law such as

$$\Delta E_{1/2}(q) = \Delta E_{1/2}(0) + Bq^2 + O(q^4) \qquad (4.3.4.13)$$

has been measured. The q dependence of $\Delta E_{1/2}$ is mainly accounted for by non-vertical transitions compatible with the band structure, the number of these transitions increasing with q (Sturm, 1982). Other mechanisms have also been suggested, such as phonons, *umklapp* processes, scattering on surfaces, *etc*.

(*c*) For large momentum transfer (*i.e.* of the order of the critical wavevector q_c), the collective modes decay into the strong electron–hole-pair channels already described giving rise to a clear increase of the damping for values of $q > q_c$.

Within this free-electron-gas description, the differential cross section for the excitation of bulk plasmons by incident electrons of velocity v is given by

$$\frac{\mathrm{d}\sigma_p}{\mathrm{d}\Omega}(\theta) = \frac{\Delta E_p}{2\pi N a_0 m_0 v^2} \frac{1}{\theta^2 + \theta_E^2}, \qquad (4.3.4.14)$$

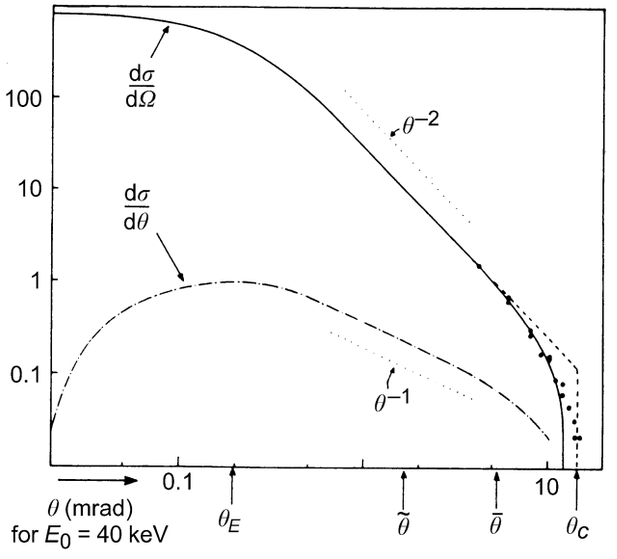

Fig. 4.3.4.14. Measured angular dependence of the differential cross section $\mathrm{d}\sigma/\mathrm{d}\Omega$ for the 15 eV plasmon loss in Al (dots) compared with a calculated curve by Ferrell (solid curve) and with a sharp cut-off approximation at θ_c (dashed curved). Also shown along the scattering angle axis, θ_E = characteristic inelastic angle defined as $\Delta E/2E_0$, $\tilde{\theta}$ = median inelastic angle defined by $\int_0^{\tilde{\theta}} (\mathrm{d}\sigma/\mathrm{d}\Omega)\,\mathrm{d}\Omega = 1/2 \int_0^{\theta_c} (\mathrm{d}\sigma/\mathrm{d}\Omega)\,\mathrm{d}\Omega$, and $\bar{\theta}$ = average inelastic angle defined by $\bar{\theta} = \int \theta(\mathrm{d}\sigma/\mathrm{d}\Omega)\,\mathrm{d}\Omega / \int (\mathrm{d}\sigma/\mathrm{d}\Omega)\,\mathrm{d}\Omega$ [courtesy of Egerton (1986)].

where N is the density of atoms per volume unit and θ_E is the characteristic inelastic angle defined as $\Delta E_p/2E_0$ in the non-relativistic description and as $\Delta E_p/\gamma m_0 v^2$ {with $\gamma = [1 - (v^2/c^2)]^{-1/2}$} in the relativistic case. The angular dependence of the differential cross section for plasmon scattering is shown in Fig. 4.3.4.14. The integral cross section up to an angle β_0 is

$$\sigma_p(\beta_0) = \int_0^{\beta_0} \left(\frac{\mathrm{d}\sigma_p}{\mathrm{d}\Omega}\right) \mathrm{d}\Omega = \frac{\Delta E_p \log(\beta_0/\theta_E)}{N a_0 m_0 v^2}. \qquad (4.3.4.15)$$

The total plasmon cross section is calculated for $\beta_0 = \theta_c = q_c/k_0$. Converted into mean free path, this becomes

$$\Lambda_p = \frac{1}{N\sigma_p} = \frac{a_0}{\theta_E} \left(\log \frac{\theta_c}{\theta_E}\right)^{-1} \quad \text{(non-relativistic formula);} \qquad (4.3.4.16)$$

and

$$\Lambda_p = \frac{a_0 \gamma m_0 v^2}{\Delta E_p} \left(\log \frac{\hbar q_c v}{1.132 \hbar \omega_p}\right)^{-1} \quad \text{(relativistic formula).} \qquad (4.3.4.17)$$

The behaviour of Λ_p as a function of the primary electron energy is shown in Fig. 4.3.4.15.

4.3.4.3.2. *Dielectric description*

The description of the bulk plasmon in the free-electron gas can be extended to any type of condensed material by introducing the dielectric response function $\varepsilon(\mathbf{q}, \omega)$, which describes the frequency and wavevector-dependent polarizability of the medium; *cf*. Daniels *et al* (1970). One associates, respectively, the ε_T and ε_L functions with the propagation of transverse and longitudinal EM modes through matter. In the small-$\mathbf{q}$ limit, these tend towards the same value:

$$\lim_{q\to 0} \varepsilon_T(\mathbf{q}, \omega) = \lim_{q\to 0} \varepsilon_L(\mathbf{q}, \omega) = \varepsilon(0, \omega).$$

As transverse dielectric functions are only used for wavevectors close to zero, the T and L indices can be omitted so that:

$$\varepsilon_L(\mathbf{q}, \omega) = \varepsilon(\mathbf{q}, \omega) \quad \text{and} \quad \varepsilon_T(\mathbf{q}, \omega) = \varepsilon(0, \omega).$$

The transverse solution corresponds to the normal propagation of EM waves in a medium of dielectric coefficient $\varepsilon(0, \omega)$, *i.e.* to

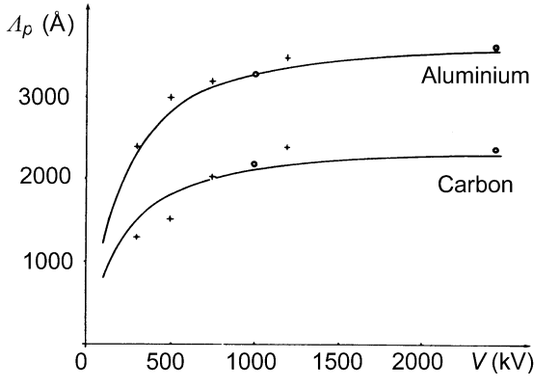

Fig. 4.3.4.15. Variation of plasmon excitation mean free path Λ_p as a function of accelerating voltage V in the case of carbon and aluminium [courtesy of Sevely (1985)].

$$\frac{q^2c^2}{\omega^2} - \varepsilon(0,\omega) = 0. \qquad (4.3.4.18)$$

For longitudinal fields, the only solution is $\varepsilon(\mathbf{q},\omega) = 0$, which is basically the dispersion relation for the bulk plasmon.

In the framework of the Maxwell description of wave propagation in matter, it has been shown by several authors [see, for instance, Ritchie (1957)] that the transfer of energy between the beam electron and the electrons in the solid is governed by the magnitude of the energy-loss function $-\mathrm{Im}[1/\varepsilon(\mathbf{q},\omega)]$, so that

$$\frac{\mathrm{d}^2\sigma}{\mathrm{d}(\Delta E)\,\mathrm{d}\Omega} = \frac{1}{N(e\pi a_0)^2}\,\frac{1}{q^2}\,\mathrm{Im}\left(-\frac{1}{\varepsilon(\mathbf{q},\omega)}\right). \qquad (4.3.4.19)$$

One can deduce (4.3.4.14) by introducing a δ function at energy loss ω_p for the energy-loss function:

$$\mathrm{Im}\left(-\frac{1}{\varepsilon(\mathbf{q},\omega)}\right) = \frac{\pi}{2}\,\omega_p\delta(\omega-\omega_p). \qquad (4.3.4.20)$$

As a consequence of the causality principle, a knowledge of the energy-loss function $-\mathrm{Im}[1/\varepsilon(\omega)]$ over the complete frequency (or energy-loss) range enables one to calculate $\mathrm{Re}[1/\varepsilon(\omega)]$ by Kramers–Kronig analysis:

$$\mathrm{Re}\frac{1}{\varepsilon(\omega)} = 1 - \frac{2}{\pi}\mathrm{PP}\int_0^\infty \mathrm{Im}\left(-\frac{1}{\varepsilon(\omega')}\right)\frac{\omega'}{\omega'^2-\omega^2}\,\mathrm{d}\omega', \qquad (4.3.4.21)$$

where PP denotes the principal part of the integral. For details of efficient practical evaluation of the above equation, see Johnson (1975).

The dielectric functions can be easily calculated for simple descriptions of the electron gas. In the Drude model, *i.e.* for a free-electron plasma with a relaxation time τ, the dielectric function at long wavelengths ($q \to 0$) is

$$\varepsilon(\omega) = \varepsilon_1(\omega) + i\varepsilon_2(\omega) = 1 - \frac{\omega_p^2}{\omega^2}\,\frac{1}{(1-1/i\omega\tau),} \qquad (4.3.4.22)$$

with $\omega_p^2 = ne^2/m\varepsilon_0$, as above. The behaviour of the different functions, the real and imaginary terms in ε, and the energy-loss function are shown in Fig. 4.3.4.16. The energy-loss term exhibits a sharp Lorentzian profile centred at $\omega = \omega_p$ and of width $1/\tau$. The narrower and more intense this plasmon peak, the more the involved valence electrons behave like free electrons.

In the Lorentz model, *i.e.* for a gas of bound electrons with one or several excitation eigenfrequencies ω_i, the dielectric function is

$$\varepsilon(\omega) = 1 + \sum_i \frac{n_i e^2}{m\varepsilon_0}\,\frac{1}{\omega_i^2 - \omega^2 + i\omega/\tau_i}, \qquad (4.3.4.23)$$

where n_i denotes the density of electrons oscillating with the frequency ω_i and τ_i is the associated relaxation time. The characteristic ε_1, ε_2, and $-\mathrm{Im}(1/\varepsilon)$ behaviours are displayed in Fig. 4.3.4.17: a typical 'interband' transition (in solid-state terminology) can be revealed as a maximum in the ε_2 function, simultaneous with a 'plasmon' mode associated with a maximum in the energy-loss function and slightly shifted to higher energies with respect to the annulation conditions of the ε_1 function.

In most practical situations, there coexist a family of n_f free electrons (with plasma frequency $\omega_p^2 = n_f e^2/m\varepsilon_0$) and one or several families of n_i bound electrons (with eigenfrequencies ω_i). The influence of bound electrons is to shift the plasma frequency towards lower values if $\omega_i > \omega_p$ and to higher values if $\omega_i < \omega_p$. As a special case, in an insulator, $n_f = 0$ and all the electrons ($n_i = n$) have a binding energy at least equal to the band gap $E_g \simeq \hbar\omega_i$, giving $\omega_p^2 = (E_g/\hbar)^2 + ne^2/m\varepsilon_0$.

This description constitutes a satisfactory first step into the world of real solids with a complex system of valence and conduction bands between which there is a strong transition rate of individual electrons under the influence of photon or electron beams. In optical spectroscopy, for instance, this transition rate, which governs the absorption coefficient, can be deduced from the calculation of the factor ε_2 as

$$\varepsilon_2(\omega) = \frac{A}{\omega^2}|M_{jj'}|^2 J_{jj'}(\omega), \qquad (4.3.4.24)$$

where $M_{jj'}$ is the matrix element for the transition from the occupied level j in the valence band to the unoccupied level j' in the conduction band, both with the same $\mathbf{k}$ value (which means for a vertical transition). $J_{jj'}(\omega)$ is the joint density of states (JDOS) with the energy difference $\hbar\omega$. This formula is also valid

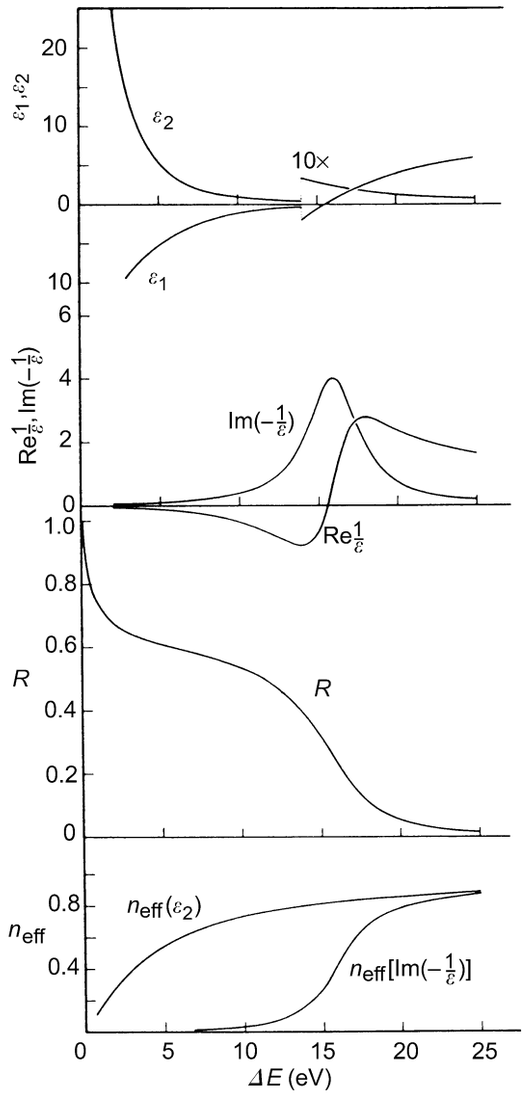

Fig. 4.3.4.16. Dielectric and optical functions calculated in the Drude model of a free-electron gas with $\hbar\omega_p = 16\,\mathrm{eV}$ and $\tau = 1.64 \times 10^{-16}\,\mathrm{s}$. R is the optical reflection coefficient in normal incidence, *i.e.* $R = [(n-1)^2 + k^2]/[(n+1)^2 + k^2]$ with n and k the real and imaginary parts of $\sqrt{\varepsilon}$. The effective numbers $n_{\mathrm{eff}}(\varepsilon_2)$ and $n_{\mathrm{eff}}[\mathrm{Im}(-1/\varepsilon)]$ are defined in Subsection 4.3.4.5 [courtesy of Daniels *et al.* (1970)].

for small-angle-scattering electron inelastic processes. When parabolic bands are used to represent, respectively, the upper part of the valence band and the lower part of the conduction band in a semiconductor, the dominant JDOS term close to the onset of the interband transitions takes the form

$$\text{JDOS} \propto (E - E_g)^{1/2}, \tag{4.3.4.25}$$

where E_g is the band-gap energy. This concept has been successfully used by Batson (1987) for the detection of gap energy variations between the bulk and the vicinity of a single misfit dislocation in a GaAs specimen. The case of non-vertical transitions involving integration over **k**-space has also been considered (Fink *et al.*, 1984; Fink & Leising, 1986).

4.3.4.3.3. *Real solids*

The dielectric constants of many solids have been deduced from a number of methods involving either primary photon or electron beams. In optical measurements, one obtains the values of ε_1 and ε_2 from a Krakers–Kronig analysis of the optical absorption and reflection curves, while in electron energy-loss measurements they are deduced from Kramers–Kronig analysis of energy-loss functions.

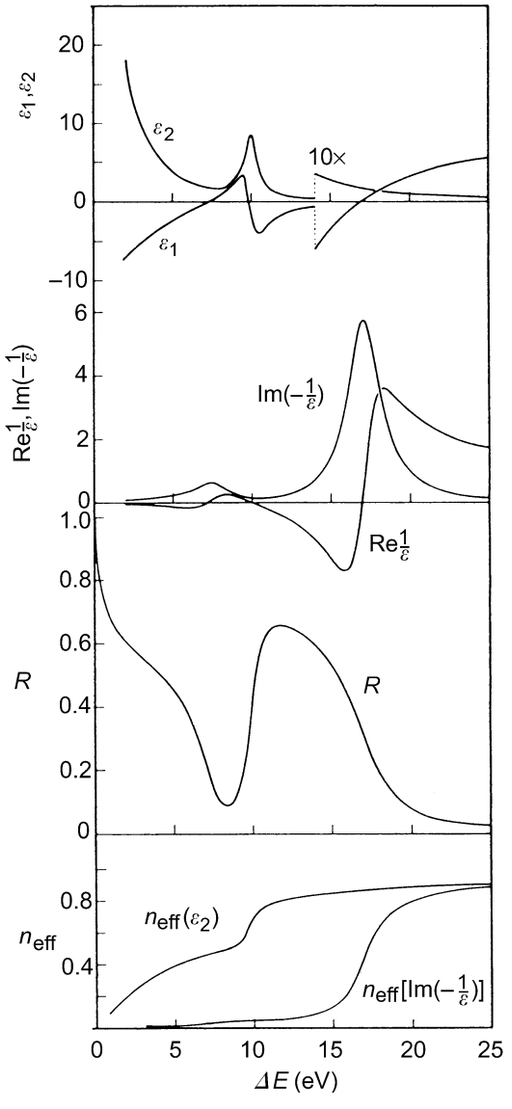

Fig. 4.3.4.17. Same as previous figure, but for a Lorentz model with an oscillator of eigenfrequency $\hbar\omega_0 = 10\,\text{eV}$ and relaxation time $\tau_0 = 6.6 \times 10^{-16}\,\text{s}$ superposed on the free-electron term [courtesy of Daniels *et al.* (1970)].

Fig. 4.3.4.18 shows typical behaviours of the dielectric and energy-loss functions.

(*a*) For a free-electron metal (Al), the Drude model is a satisfactory description with a well defined narrow and intense maximum of $\text{Im}(-1/\varepsilon)$ corresponding to the collective plasmon excitation together with typical conditions $\varepsilon_1 \simeq \varepsilon_2 \simeq 0$ for this energy $\hbar\omega_p$. One also notices a weak interband transition below 2 eV.

(*b*) For transition and noble metals (such as Au), the results strongly deviate from the free-electron gas function as a consequence of intense interband transitions originating mostly from the partially or fully filled *d* band lying in the vicinity of, or just below, the Fermi level. There is no clear condition for satisfying the criterion of plasma excitation ($\varepsilon = 0$) so that the collective modes are strongly damped. However, the higher-lying peak is more generally of a collective nature because it coincides with the exhaustion of all oscillator strengths for interband transitions.

(*c*) Similar arguments can be developed for a semiconductor (InSb) or an insulator (Xe solid). In the first case, one detects a few interband transitions at small energies that do not prevent the occurrence of a pronounced volume plasmon peak rather similar to the free-electron case. The difference between the gap and the plasma energy is so great that the valence electrons behave collectively as an assembly of free particles. In contrast, for wide gap insulators (alkali halides, oxides, solid rare gases), a number of peaks are seen, owing to different interband transitions and exciton peaks. Excitons are quasi-particles consisting of a conduction-band electron and a valence-band hole bound to each other by Coloumb interaction. One observes the existence of a band gap [no excitation either in ε_2 or in $\text{Im}(-1/\varepsilon)$ below a given critical value E_g] and again the higher-lying peak is generally of a rather collective nature.

Čerenkov radiation is emitted when the velocity v of an electron travelling through a medium exceeds the speed of light for a particular frequency in this medium. The criterion for Čerenkov emission is

$$\varepsilon_1(\omega) > \frac{c^2}{v^2} = \beta^{-2}. \tag{4.3.4.26}$$

In an insulator, ε_1 is positive at low energies and can considerably exceed unity, so that a 'radiation peak' can be detected in the corresponding energy-loss range (between 2 and 4 eV in Si, Ge, III–V compounds, diamond, ...); see Von Festenberg (1968), Kröger (1970), and Chen & Silcox (1971). The associated scattering angle, $\theta \simeq \lambda_{\text{el}}/\lambda_{\text{ph}} \simeq 10^{-5}\,\text{rad}$ for high-energy electrons, is very small and this contribution can only be detected using a limited forward-scattering angular acceptance.

In an *anisotropic* crystal, the dielectric function has the character of a tensor, so that the energy-loss function is expressed as

$$\text{Im}\left(-\frac{1}{\sum_i \sum_j \varepsilon_{ij}\, q_i\, q_j}\right). \tag{4.3.4.27}$$

If it is transformed to its orthogonal principal axes $(\varepsilon_{11}, \varepsilon_{22}, \varepsilon_{33})$, and if the **q** components in this system are q_1, q_2, q_3, the above expression simplifies to

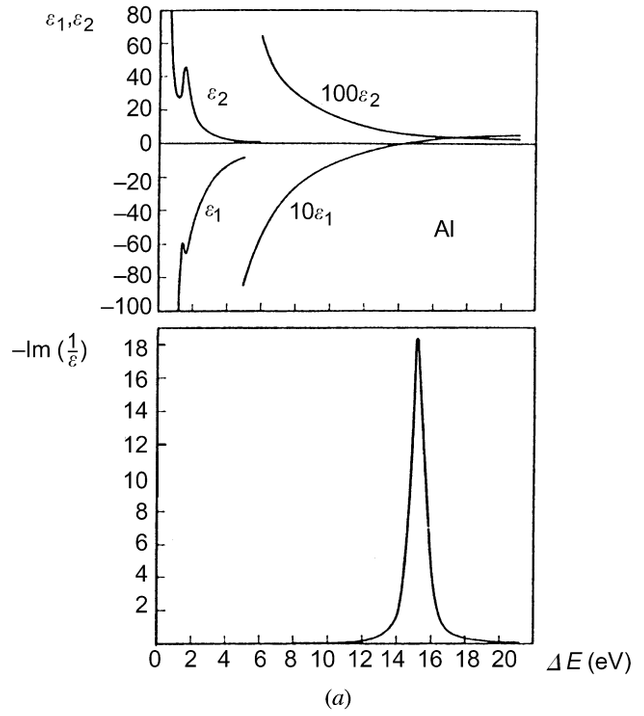

(a)

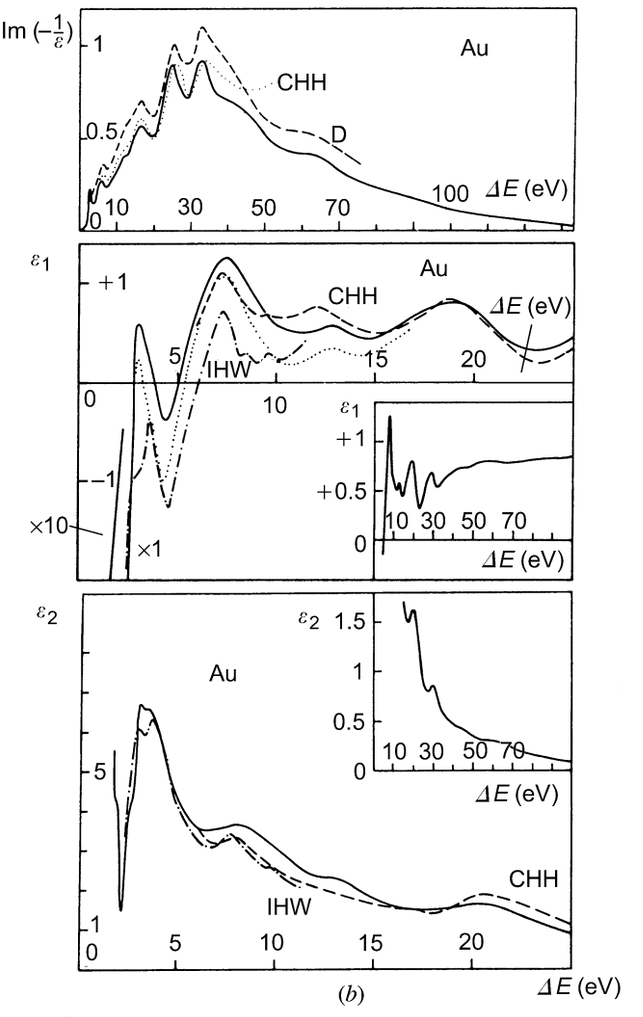

(b)

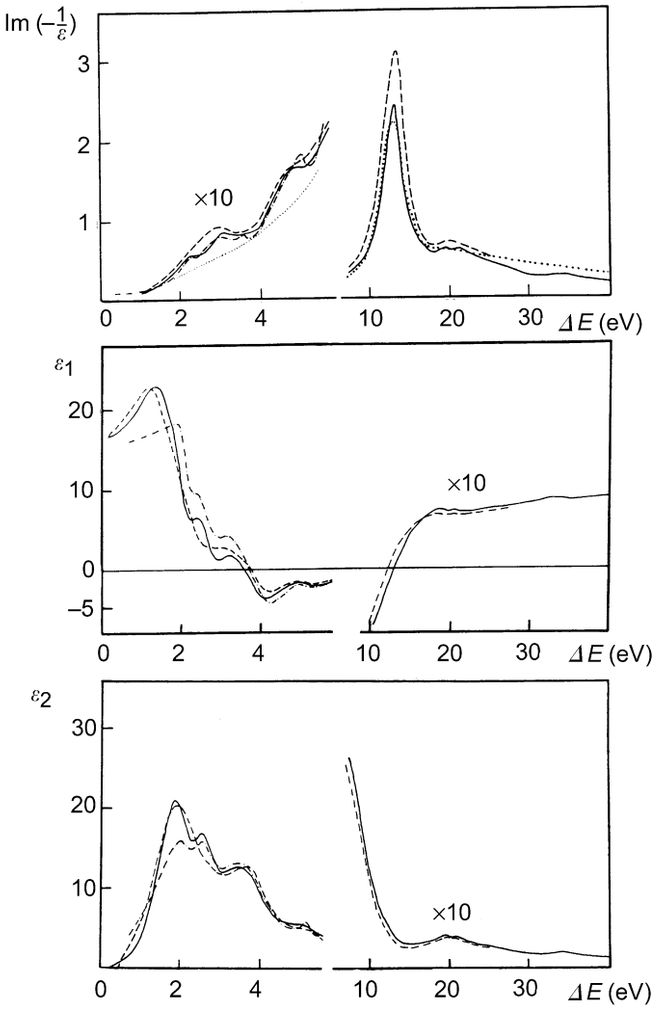

(c)

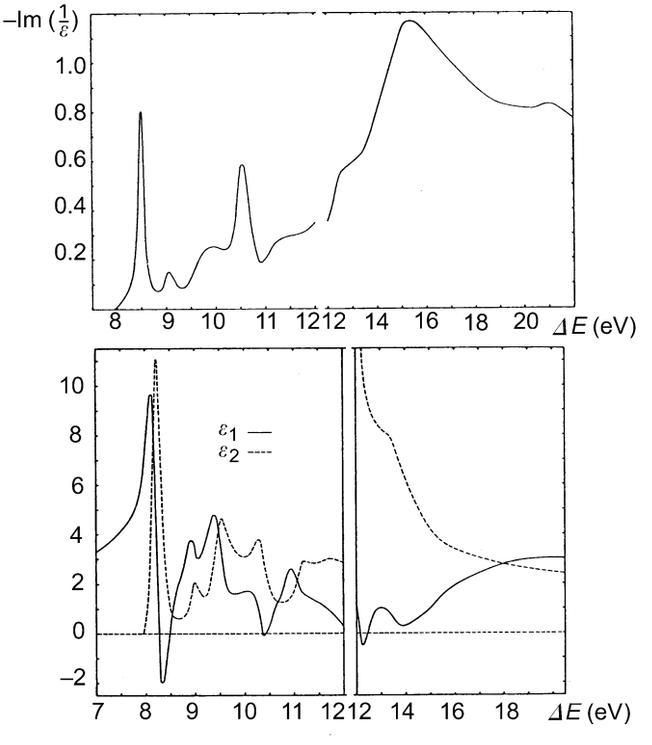

(d)

Fig. 4.3.4.18. Dielectric coefficients ε_1, ε_2 and $\mathrm{Im}(-1/\varepsilon)$ from a collection of typical real solids: (*a*) aluminium [courtesy of Raether (1965)]; (*b*) gold [courtesy of Wehenkel (1975)]; (*c*) InSb [courtesy of Zimmermann (1976)]; (*d*) solid xenon at *ca* 5 K [courtesy of Keil (1968)].

$$\mathrm{Im}\left(-\frac{1}{\sum_i \varepsilon_{ii} q_i^2}\right). \qquad (4.3.4.28)$$

In a uniaxial crystal, such as a graphite, $\varepsilon_{11} = \varepsilon_{22} = \varepsilon_\perp$ and $\varepsilon_{33} = \varepsilon_\parallel$ (*i.e.* parallel to the c axis):

$$\varepsilon(\mathbf{q}, \omega) = \varepsilon_\perp \sin^2\theta + \varepsilon_\parallel \cos^2\theta, \qquad (4.3.4.29)$$

where θ is the angle between $\mathbf{q}$ and the c axis. The spectrum depends on the direction of $\mathbf{q}$, either parallel or perpendicular to the c axis, as shown in Fig. 4.3.4.19 from Venghaus (1975). These experimental conditions may be achieved by tilting the graphite layer at 45° with respect to the incident axis, and recording spectra in two directions at $\pm\theta_E$ with respect to it (see Fig. 4.3.4.20).

4.3.4.3.4. *Surface plasmons*

Volume plasmons are longitudinal waves of charge density propagating through the bulk of the solid. Similarly, three exist longitudinal waves of charge density travelling along the surface between two media A and B (one may be a vacuum): these are the surface plasmons (Kliewer & Fuchs, 1974). Boundary conditions imply that

$$\varepsilon_A(\omega) + \varepsilon_B(\omega) = 0. \qquad (4.3.4.30)$$

The corresponding charge-density fluctuation is contained within the (**x**) boundary plane, z being normal to the surface:

$$\rho(\mathbf{x}, z) \simeq \cos(\mathbf{q}\cdot\mathbf{x} - \omega t)\delta(z), \qquad (4.3.4.31)$$

and the associated electrostatic potential oscillates in space and time as

$$\varphi(\mathbf{x}, z)\, \alpha \cos(\mathbf{q}\cdot\mathbf{x} - \omega t)\exp(-q|z|). \qquad (4.3.4.32)$$

The characteristic energy ω_s of this surface mode is estimated in the free electron case as:

In the planar interface case:

$$\left.\begin{aligned}
&\omega_s = \frac{\omega_p}{\sqrt{2}} \\
&\quad \text{(interface metal–vacuum);} \\
&\omega_s = \frac{\omega_p}{(1+\varepsilon_d)^{1/2}} \\
&\quad \text{(interface metal–dielectric of constant } \varepsilon_d\text{);} \\
&\omega_s = \left(\frac{\omega_{p_A}^2 + \omega_{p_B}^2}{2}\right)^{1/2} \\
&\quad \text{(interface metal } A\text{–metal } B\text{).}
\end{aligned}\right\} \qquad (4.3.4.33)$$

In the spherical interface case:

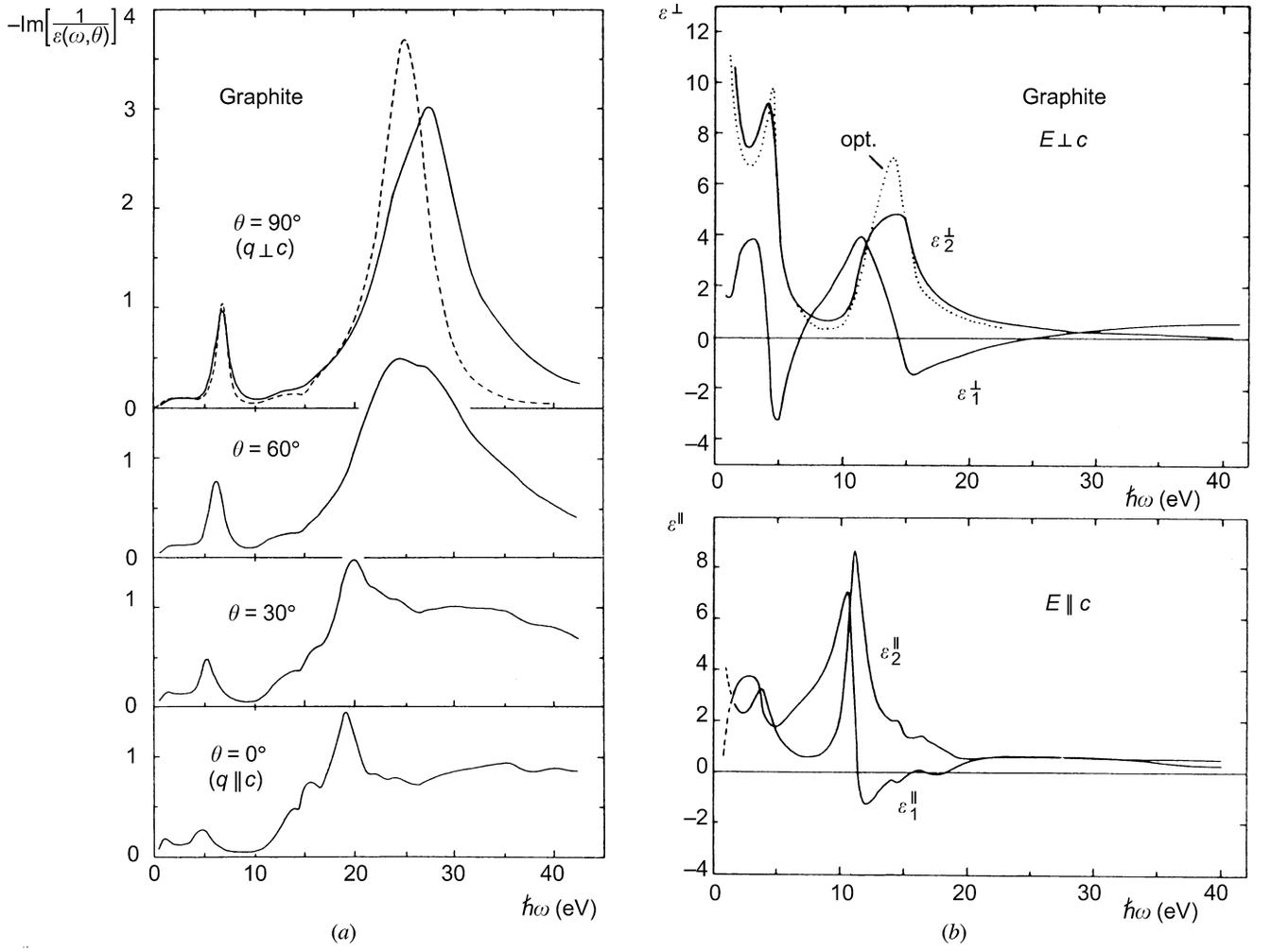

Fig. 4.3.4.19. Dielectic functions in graphite derived from energy losses for $E \perp c$ (*i.e.* the electric field vector being in the layer plane) and for $E \| c$ [from Daniels *et al.* (1970)]. The dashed line represents data extracted from optical reflectivity measurements [from Taft & Philipp (1965)].

$$(\omega_s)_l = \frac{\omega_p}{[(2l+1)/l]^{1/2}} \qquad (4.3.4.34a)$$

(metal sphere in vacuum – the modes are now quantified following the l quantum number in spherical geometry);

$$(\omega_s)_l = \frac{\omega_p}{[(2l+1)/(l+1)]^{1/2}} \qquad (4.3.4.34b)$$

(spherical void within metal).

Thin-film geometry:

$$(\omega_s)^{\pm} = \omega_p \left[\frac{1 \pm \exp(-qt)}{1+\varepsilon_d}\right]^{1/2} \qquad (4.3.4.35)$$

(metal layer of thickness t embedded in dielectric films of constant ε_d). The two solutions result from the coupling of the oscillations on the two surfaces, the electric field being symmetric for the $(\omega_s)^-$ mode and antisymmetric for the $(\omega_s)^+$.

In a real solid, the surface plasmon modes are determined by the roots of the equation $\varepsilon(\omega_s) = -1$ for vacuum coating [or $\varepsilon(\omega_s) = -\varepsilon_d$ for dielectric coating].

The probability of surface-loss excitation P_s is mostly governed by the $\mathrm{Im}\{-1/[1+\varepsilon(\omega)]\}$ energy-loss function, which is analogous for surface modes to the bulk $\mathrm{Im}\{-1/[\varepsilon(\omega)]\}$ energy-loss function. In normal incidence, the differential scattering cross section $\mathrm{d}P_s/\mathrm{d}\Omega$ is zero in the forward direction, reaches a maximum for $\theta = \pm\theta_E/3^{1/2}$, and decreases as θ^{-3} at large angles. In non-normal incidence, the angular distribution is asymmetrical, goes through a zero value for momentum transfer $\hbar\mathbf{q}$ in a direction perpendicular to the interface, and the total probability increases as

$$P_s(\varphi) = \frac{P_s(O)}{\cos\varphi}, \qquad (4.3.4.36)$$

where φ is the incidence angle between the primary beam and the normal to the surface. As a consequence, the probability of producing one (and several) surface losses increases rapidly for grazing incidences.

4.3.4.4. *Excitation spectrum of core electrons*

4.3.4.4.1. *Definition and classification of core edges*

As for any core-electron spectroscopy, EELS spectroscopy at higher energy losses mostly deals with the excitation of well defined atomic electrons. When considering solid specimens, both initial and final states in the transition are actually eigenstates in the solid state. However, the initial wavefunction can be considered as purely atomic for core excitations. As a first consequence, one can classify these transitions as a function of the parameters of atomic physics: Z is the atomic number of the element; n, l, and $j = l + s$ are the quantum numbers describing the subshells from which the electron has been excited. The spectroscopy notation used is shown in Fig. 4.3.4.21. The list of major transitions is displayed as a function of Z and E_c in Fig. 4.3.4.22.

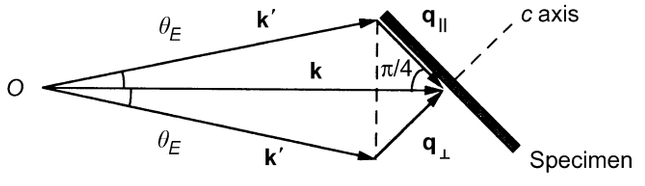

Fig. 4.3.4.20. Geometric conditions for investigating the anisotropic energy-loss function.

Core excitations appear as edges superimposed, from the threshold energy E_c upwards, above a regularly decreasing background. As explained below, the basic matrix element governing the probability of transition is similar for optical absorption spectroscopy and for small-angle-scattering EELS spectroscopy. Consequently, selection rules for dipole transitions define the dominant transitions to be observed, *i.e.*

$$l' - l = \Delta l = \pm 1 \quad \text{and} \quad j' - j = \Delta j = 0, \pm 1. \qquad (4.3.4.37)$$

This major rule has important consequences for the edge shapes to be observed: approximate behaviours are also shown in Fig. 4.3.4.22. A very useful library of core edges can be found in the EELS atlas (Ahn & Krivanek, 1982), from which we have selected the family of edges gathered in Fig. 4.3.4.23. They display the following typical profiles:

(i) *K edges for low-Z elements* ($3 \leq Z \leq 14$). The carbon K edge occurring at 284 eV is a nice example with a clear hydrogenic or saw-tooth profile and fine structures on threshold depending on the local environment (amorphous, graphite, diamond, organic molecules, ...); see Isaacson (1972*a*,*b*).

(ii) *$L_{2,3}$ edges for medium-Z elements* ($11 \lesssim Z \lesssim 45$). The $L_{2,3}$ edges exhibit different shapes when the outer occupied shell changes in nature: a delayed profile is observed as long as the first vacant d states are located, along the energy scale, rather above the Fermi level (sulfur case). When these d states coincide with the first accessible levels, sharp peaks, generally known as 'white lines', appear at threshold (this is the case for transition elements with the Fermi level inside the d band). These lines are generally split by the spin-orbit term on the initial level into $2p^{3/2}$ and $2p^{1/2}$ (or L_3 and L_2) terms. For higher-Z elements, the bound d levels are fully occupied, and

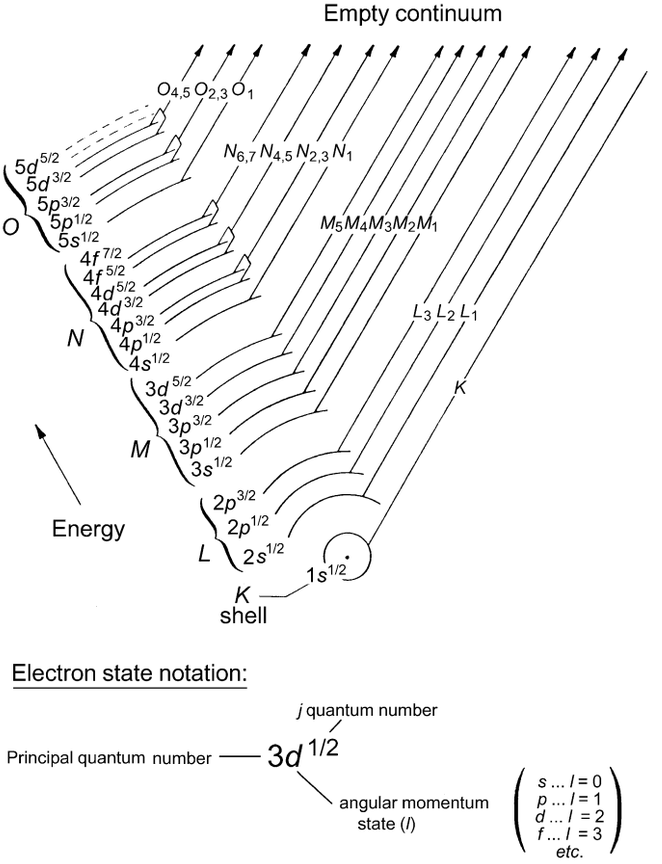

Fig. 4.3.4.21. Definition of electron shells and transitions involved in core-loss spectroscopy [from Ahn & Krivanek (1982)].

no longer contribute as host orbitals for the excited $2p$ electrons. One finds again a more traditional hydrogenic profile (such as for the germanium case).

(iii) *$M_{4,5}$ edges for heavier-Z elements* ($37 \lesssim Z \lesssim 83$). A sequence of $M_{4,5}$ edge profiles, rather similar to $L_{2,3}$ edges, is observed, the difference being that one then investigates the density of the final *f* states. White lines can also be detected when the *f* levels lie in the neighbourhood of the Fermi level, *e.g.* for rare-earth elements.

The deeper accessible signals, for incident electrons in the range of 100–400 kV primary voltage, lie between 2500 and 3000 eV, which corresponds roughly to the middle of the second row of transition elements (Mo–Ru) for the $L_{2,3}$ edge and to the very heavy metals (Pb–Bi) for the $M_{4,5}$ edge.

(iv) A final example in Fig. 4.3.4.23 concerns one of these resonant peaks associated with the excitation of levels just below the conduction band. These are features with high intensity of the same order or even superior to that of plasmons of conduction

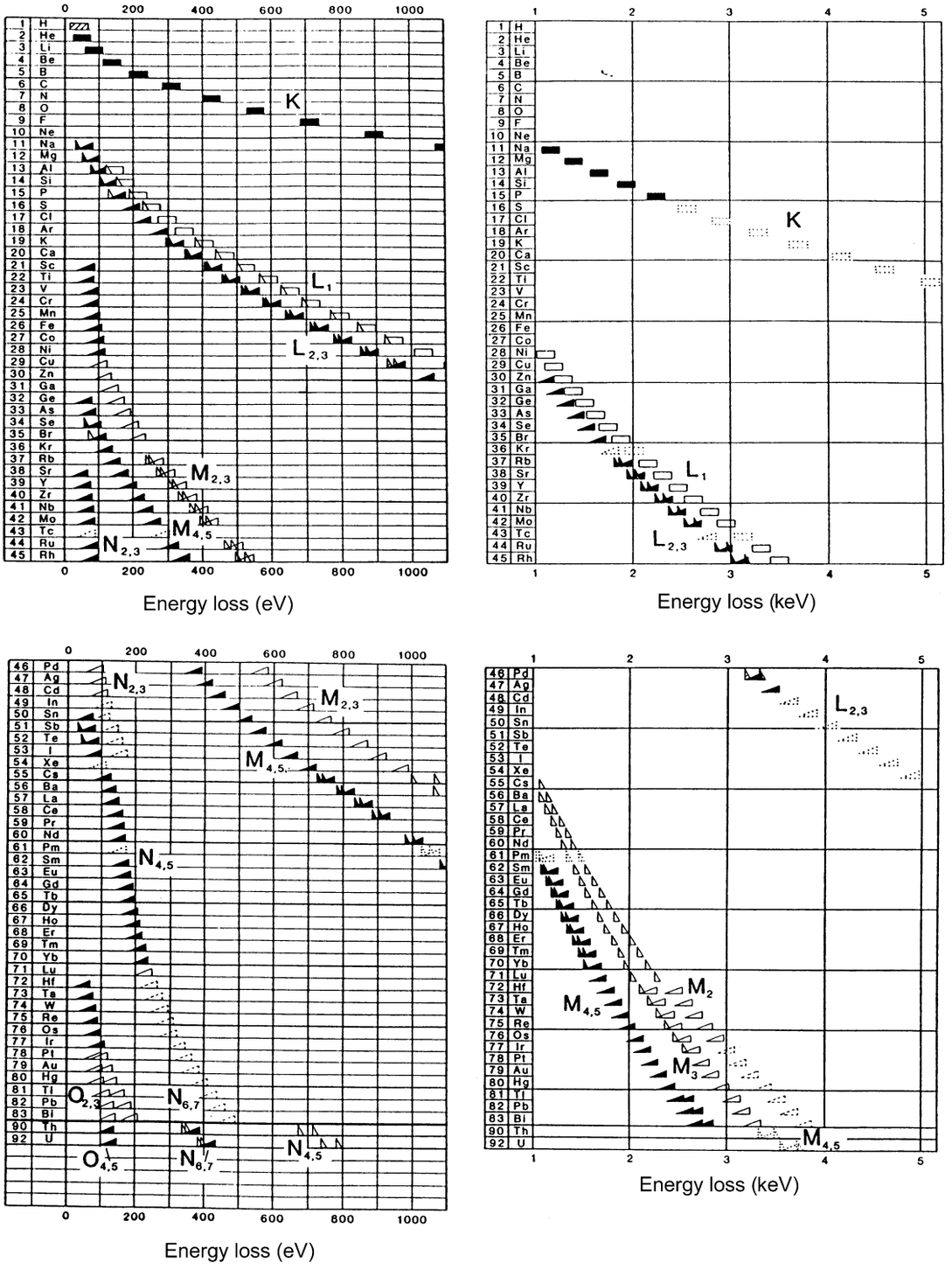

Fig. 4.3.4.22. Chart of edges encountered in the 50 eV up to 3 keV energy-loss range with symbols identifying the types of shapes [see Ahn & Krivanek (1982) for further comments].

band electrons previously described in Subsection 4.3.4.3. It occurs with the $M_{2,3}$ level for the first transition series, with the $N_{2,3}$ level for the second series (for example, strontium in Fig. 4.3.4.23) or with the $O_{2,3}$ level for the third series, including the rare-earth elements. The shape varies gradually from a plasmon-like peak with a short lifetime to an asymmetric Fano-type profile, a consequence of the coupling between discrete and continuum final states of the same energy (Fano, 1961).

4.3.4.4.2. *Bethe theory for inelastic scattering by an isolated atom (Bethe, 1930; Inokuti, 1971, 1979)*

As a consequence of the atomic nature of the excited wavefunction in core-loss spectroscopy, the first step involves deriving a useful theoretical expression for inelastic scattering by an isolated atom. The differential cross section for an electron of wavevector $\mathbf{k}$ to be scattered into a final plane wave of vector $\mathbf{k}'$, while promoting one atomic electron from ψ_0 to ψ_n, is given in a one-electron excitation description by

$$\frac{\mathrm{d}\sigma_n}{\mathrm{d}\Omega\,\mathrm{d}(\Delta E)} = \left(\frac{m_0}{2\pi\hbar^2}\right)^2 \frac{k'}{k} |\langle \psi_n \mathbf{k}' | V(\mathbf{r}) | \psi_0 \mathbf{k} \rangle|^2; \qquad (4.3.4.38)$$

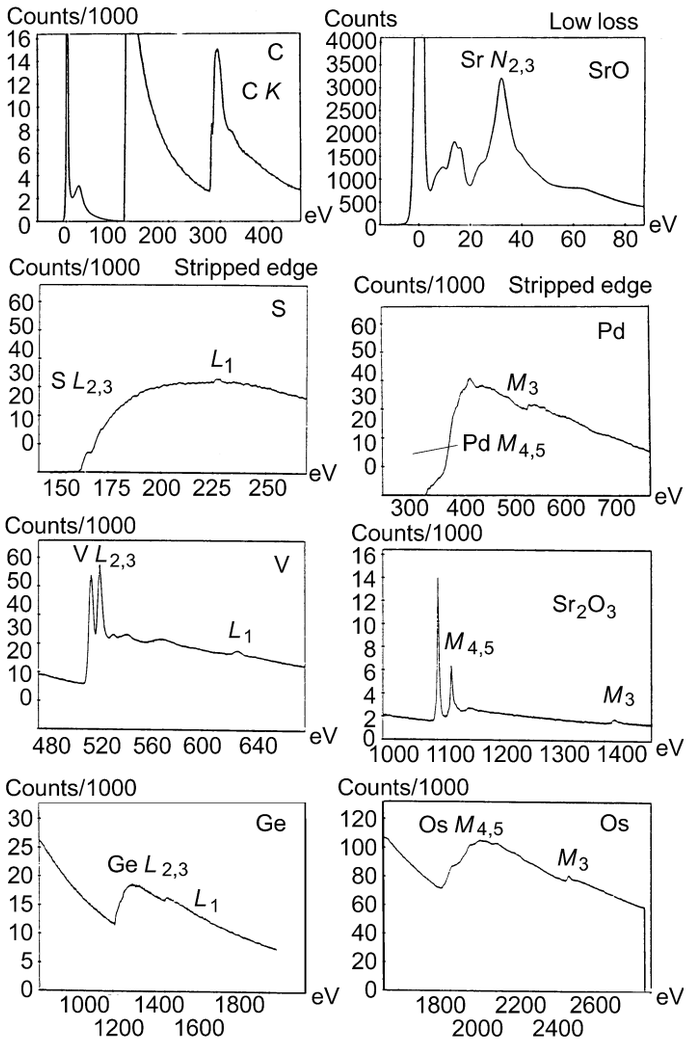

Fig. 4.3.4.23. A selection of typical profiles ($K, L_{2,3}, M_{4,5}$, and $N_{2,3}$) illustrating the most important behaviours encountered on major edges through the Periodic Table. A few edges are displayed prior to and others after background stripping. [Data extracted from Ahn & Krivanek (1982).]

see, for instance, Landau & Lifchitz (1966) and Mott & Massey (1952). The potential $V(\mathbf{r})$ corresponds to the Coulomb interaction with all charges (both in the nucleus and in the electron cloud) of the atom. The momentum change in the scattering event is $\hbar\mathbf{q} = \hbar(\mathbf{k} - \mathbf{k}')$. The final-state wavefunction is normalized per unit energy range. The orthogonality between initial- and final-state wavefunctions restricts the inelastic scattering to the only interactions with atomic electrons:

$$\frac{\mathrm{d}\sigma_n}{\mathrm{d}\Omega\,\mathrm{d}(\Delta E)} = \frac{4\gamma^2}{a_0^2 q^4} \frac{k'}{k} |\mathscr{E}_n(\mathbf{q}, \Delta E)|^2. \qquad (4.3.4.39)$$

The first part of the above expression has the form of Rutherford scattering. γ is introduced to deal, to a first approximation, with relativistic effects. The ratio k'/k is generally assumed to be equal to unity. This kinematic scattering factor is modified by the second term, or matrix element, which describes the response of the atomic electrons:

$$\mathscr{E}_n(\mathbf{q}, \Delta E) = \left\langle \psi_n \left| \sum_j \exp(i\mathbf{q}\cdot\mathbf{r}_j) \right| \psi_0 \right\rangle, \qquad (4.3.4.40)$$

where the sum extends over all atomic electrons at positions $\mathbf{r}_j$. The dimensionless quantity is known as the *inelastic form factor*.

For a more direct comparison with photoabsorption measurements, one introduces the generalized oscillator strength (GOS) as

$$\frac{\mathrm{d}f(\mathbf{q}, \Delta E)}{\mathrm{d}(\Delta E)} = \frac{\Delta E}{R} \frac{|\mathscr{E}_n(\mathbf{q}, \Delta E)|^2}{(qa_0)^2} \qquad (4.3.4.41)$$

for transitions towards final states ψ_ε in the continuum [ΔE is then the energy difference between the core level and the final state of kinetic energy ε above the Fermi level, scaled in energy to the Rydberg energy (R)]. Also,

$$f_n(\mathbf{q}) = \frac{E_n}{R} \frac{|\mathscr{E}_n(\mathbf{q})|^2}{(qa_0)^2} \qquad (4.3.4.42)$$

for transition towards bound states. In this case, E_n is the energy difference between the two states involved.

The generalized oscillator strength is a function of both the energy ΔE and the momentum $\hbar\mathbf{q}$ transferred to the atom. It is displayed as a three-dimensional surface known as the Bethe surface (Fig. 4.3.4.24), which embodies all information concerning the inelastic scattering of charged particles by atoms. The angular dependence of the cross section is proportional to

$$\frac{1}{q^2} \frac{\mathrm{d}f(\mathbf{q}, \Delta E)}{\mathrm{d}(\Delta E)}$$

at a given energy loss ΔE.

In the small-angle limit ($qr_c \ll 1$, where r_c is the average radius of the initial orbital), the GOS reduces to the optical oscillator strength

$$\frac{\mathrm{d}f(\mathbf{q}, \Delta E)}{\mathrm{d}(\Delta E)} \rightarrow \frac{\mathrm{d}f(0, \Delta E)}{\mathrm{d}(\Delta E)}$$

and

$$\mathscr{E}_n(\mathbf{q}, \Delta E) \rightarrow \mathscr{E}_n(0, \Delta E) = q^2 \left| \left\langle \psi_n \left| \sum_j \mathbf{u}\cdot\mathbf{r}_j \right| \psi_0 \right\rangle \right|^2, \qquad (4.3.4.43)$$

where $\mathbf{u}$ is the unit vector in the $\mathbf{q}$ direction. When one is concerned with a given orbital excitation, the sum over $\mathbf{r}_j$ reduces to a single term $\mathbf{r}$ for this electron. With some elementary calculations, the resulting cross section is

$$\frac{\mathrm{d}^2\sigma}{\mathrm{d}\Omega\,\mathrm{d}(\Delta E)} = \frac{4\gamma^2 R}{\Delta E\,k^2}\,\frac{1}{\theta^2+\theta_E^2}\,\frac{\mathrm{d}f(0,\Delta E)}{\mathrm{d}(\Delta E)}. \qquad (4.3.4.44)$$

The major angular dependence is contained, as in the low-loss domain, in the Lorentzian factor $(\theta^2+\theta_E^2)^{-1}$, with the characteristic inelastic angle θ_E being again equal to $\Delta E/\gamma m_0 v^2$. Over this reduced scattering-angle domain, known as the dipole region, the GOS is approximately constant and the inner-shell EELS spectrum is directly proportional to the photoabsorption cross section $\sigma_{\rm opt}$, whose data can be used to test the results of single-atom calculations. For larger scattering angles, Fig. 4.3.4.24 exhibits two distinct behaviours for energy losses just above the edge ($\mathrm{d}f/\mathrm{d}\Delta E$ drops regularly to zero), and for energy losses much greater than the core-edge threshold. In the latter case, the oscillator strength is mostly concentrated in the Bethe ridge, the maximum of which occurs for:

$$\left.\begin{aligned}(qa_0)^2 &= \frac{\Delta E}{R} \quad \text{(non-relativistic formula)},\\ (qa_0)^2 &= \frac{\Delta E}{R}\frac{(\Delta E)^2}{2m_0c^2R} \quad \text{(relativistic formula)}.\end{aligned}\right\} \qquad (4.3.4.45)$$

This contribution at large scattering angles is equivalent to direct knock-on collisions of free electrons, *i.e.* to the curve $\Delta E = \hbar^2 q^2/2m_0$ lying in the middle of the valence-electron–hole excitations continuum (see Fig. 4.3.4.13). The non-zero width of the Bethe ridge can be used as an electron Compton profile to analyse the momentum distribution of the atomic electrons [see also §4.3.4.4.4(*c*)].

The energy dependence of the cross section, responsible for the various edge shapes discussed in §4.3.4.4.1, is governed by

$$\frac{1}{\Delta E}\,\frac{\mathrm{d}f(\mathbf{q},\Delta E)}{\mathrm{d}(\Delta E)},$$

i.e. it corresponds to sections through the Bethe surface at constant $\mathbf{q}$. Within the general theory described above, various models have been developed for practical calculations of energy differential cross sections.

The hydrogenic model due to Egerton (1979) is an extension of the quantum-mechanical calculations for a hydrogen atom to inner-shell electron excitations in an atom Z by introduction of some useful parametrization (effective nuclear charge, effective threshold energy). It is applied in practice for K and $L_{2,3}$ shells.

In the Hartree–Slater (or Dirac–Slater) description, one calculates the final continuum-state wavefunction in a self-consistent central field atomic potential (Leapman, Rez & Mayers, 1980; Rez, 1989). The radial dependence of these wavefunctions is given by the solution of a Schrödinger equation with an effective potential:

$$V_{\rm eff}(r) = V(r) + \frac{l'(l'+1)\hbar^2}{2m_0r^2}, \qquad (4.3.4.46)$$

where $[l'(l'+1)\hbar^2]/2m_0r^2$ is the centrifugal potential, which is important for explaining the occurrence of delayed maxima in spectra involving final states of higher l'. This approach is now useful for any major K, $L_{2,3}$, $M_{4,5}$, ... edge, as illustrated by Ahn & Rez (1985) and more specifically in rare-earth elements by Manoubi, Rez & Colliex (1989).

These differential cross sections can be integrated over the relevant angular and energy domains to provide data comparable with experimental measurements. In practice, one records the energy spectral distribution of electrons scattered into all angles up to the acceptance value β of the collection aperture. The integration has therefore to be made from $q_{\rm min} \simeq k\theta_E$ for the zero scattering-angle limit, up to $q_{\rm max} \simeq k\beta$. Fig. 4.3.4.25 shows how such calculated profiles can be used for fitting experimental data.

Setting $\beta = \pi$ [or equal to an effective upper limit $\theta_{\rm max} \simeq (\Delta E/E_0)^{1/2}$ corresponding to the criterion $q_{\rm max}r \simeq 1$], the integral cross section is the total cross section for the excitation of a given core level. These ionization cross sections are required for quantification in all analytical techniques using core-level excitations and de-excitations, such as EELS, Auger electron spectroscopy, and X-ray microanalysis (see Powell, 1976, 1984). A convenient way of comparing total cross sections is to rewrite the Bethe asymptotic cross section as

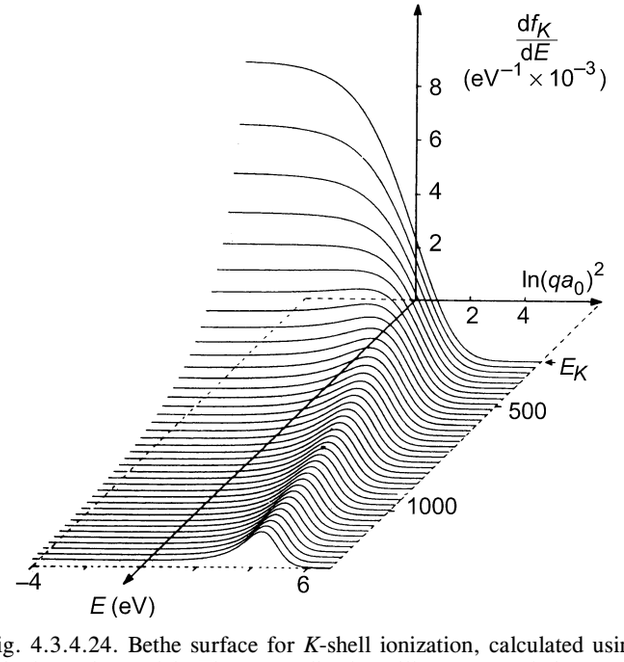

Fig. 4.3.4.24. Bethe surface for K-shell ionization, calculated using a hydrogenic model. The generalized oscillator strength is zero for energy loss E below the threshold E_K. The horizontal coordinate is related to scattering angle through q [from Egerton (1979)].

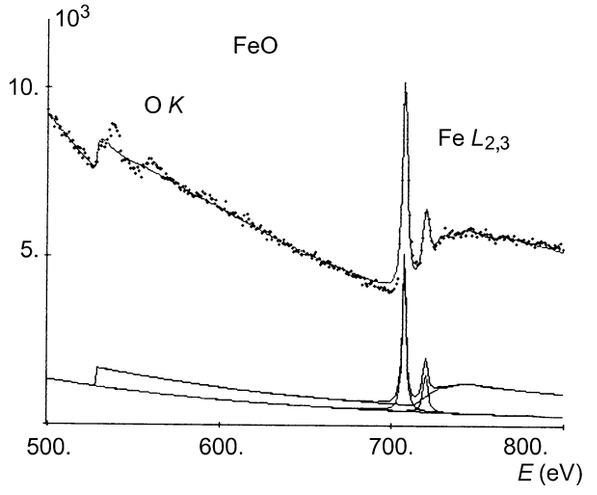

Fig. 4.3.4.25. A novel technique for simulating an energy-loss spectrum with two distinct edges as a superposition of theoretical contributions (hydrogenic saw-tooth for O K, Lorentzian white lines and delayed continuum for Fe $L_{2,3}$ calculated with the Hartree–Slater description). The best fit between the experimental and the simulated spectra is shown; it can be used to evaluate the relative concentration of the two elements [see Manoubi *et al.* (1990)].

$$\sigma_{nl}E_{nl}^2 = 6.51 \times 10^{-14} Z_{nl} b_{nl} \frac{\log(C_{nl}U_{nl})}{U_{nl}}, \qquad (4.3.4.47)$$

when the result is given in cm^2, σ_{nl} is the total cross section per atom or molecule or ionization of the *nl* subshell with edge energy E_{nl}, Z_{nl} is the number of electrons on the *nl* level, and U_{nl} is the overvoltage defined as E_0/E_{nl}. b_{nl} and c_{nl} are two parameters representing phenomenologically the average number of electrons involved in the excitation and their average energy loss (one finds for the major K and $L_{2,3}$ edges $b_{nl} \simeq 0.6$–0.9 and $c_{nl} \simeq 0.5$–0.7). These values are in practice estimated from plots of curves $\sigma_{nl}E_{nl}^2U_{nl}$ as a function of $\log U_{nl}$, known as Fano plots. From least-squares fits to linear regions, one can evaluate the values of b_{nl} (slope of the curves) and of $\log c_{nl}$ (coordinate at the origin) for various elements and shells. However, it has been shown more recently (Powell, 1989) that the interpretation of Fano plots is not always simple, since they typically display two linear regions. It is only in the linear region for the higher incident energies that the plots show the asymptotic Bethe dependence with the slope directly related to the optical data. At lower incident energies, another linear region is found with a slope typically 10–20% greater. Despite great progress over the last two decades, more cross-section data, either theoretical or experimental, are still required to improve to the 1% level the accuracy in all techniques using these signals.

4.3.4.4.3. *Solid-state effects*

The characteristic core edges recorded from solid specimens display complex structures different from those described in atomic terms. Moreover, their detailed spectral distributions depend on the type of compound in which the element is present (Leapman, Grunes & Fejes, 1982; Grunes, Leapman, Wilker, Hoffmann & Kunz, 1982; Colliex, Manoubi, Gasgnier & Brown, 1985). Modifications induced by the local solid-state environment concern (see Fig. 4.3.4.26) the following:

(*a*) *The threshold* (or edge itself), which may vary in position, slope, and associated fine structures. From photoelectron spectroscopies (UPS, XPS), an edge displacement along the energy scale is known as a 'chemical shift': it is due to a shift in the energy of the initial level as a consequence of the atomic potential modifications induced by valence-electron charge transfer (*e.g.* from metal to oxide). EELS is actually a two-level spectroscopy and the observed changes at edge onset concern both initial and final states. Consequently, measured shifts are due to a combination of core-level energy shift with bandgap and exciton creation. Some important shifts have been measured in EELS such as:

– carbon K: 284 to 288 eV from graphite to diamond;

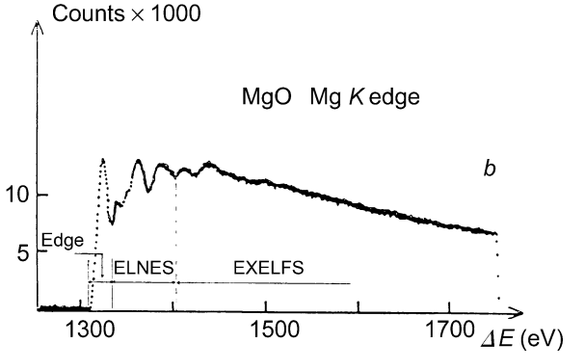

Fig. 4.3.4.26. Definition of the different fine structures visible on a core-loss edge.

– aluminium $L_{2,3}$: 73 to 77 eV from metal to Al_2O_3;

– silicon $L_{2,3}$: 99.5 to 106 eV from Si to SiO_2.

However, 'chemical shift' constitutes a simplified description of the more complex changes that may occur at a given threshold in various compounds. It assumes a rigid translation of the edge, but in most cases the onset changes in shape and there are no simple features to correlate through the different spectra. This remark is more relevant with the increased energy resolution that is now available. With a sub-eV value, extra peaks or splittings can frequently be detected on edges that exhibit simple shapes when recorded at lower resolution. Among others, the L_{32} white lines in transition metals show different behaviours when involved in various environments:

– crystal-field-induced splitting for each line in the oxides Sc_2O_3, TiO_2 when compared with the metal (see Fig. 4.3.4.27).

– relative change in L_3/L_2 intensity ratio between different ionic species [most important when the occupancy degree n for the d band is of the order of 5, *i.e.* around the middle of the transition series, *e.g.* Mn and Fe oxides; see for instance, Rask, Miner & Buseck (1987) and Rao, Thomas, Williams & Sparrow (1984)].

– presence of a narrow white line instead of a hydrogenic profile when the electron transfer from the metal to its ligand induces the existence of vacant d states at the Fermi level (CuO compared with Cu, see Fig. 4.3.4.28).

(*b*) *The near-edge fine structures* (ELNES), which extend over the first 20 or 30 eV above threshold (Taftø & Zhu, 1982; Colliex *et al.*, 1985). These are very similar to XANES structures in X-ray photoabsorption spectroscopy: they mostly reflect the spectral distribution of vacant accessible levels and are consequently very sensitive to site symmetry and charge transfer. Several approaches have been proposed to interpret them. A molecular-orbital description [*e.g.* Fischer (1970) or Tossell, Vaughan & Johnson (1974)] classifies the energy levels, both occupied and unoccupied, for clusters comprising the central excited ion and its first shell of neighbours. Its major success lies in the interpretation of level splitting on edges.

A one-electron band calculation constitutes a second step with noticeable successes in the case of metals (Müller, Jepsen &

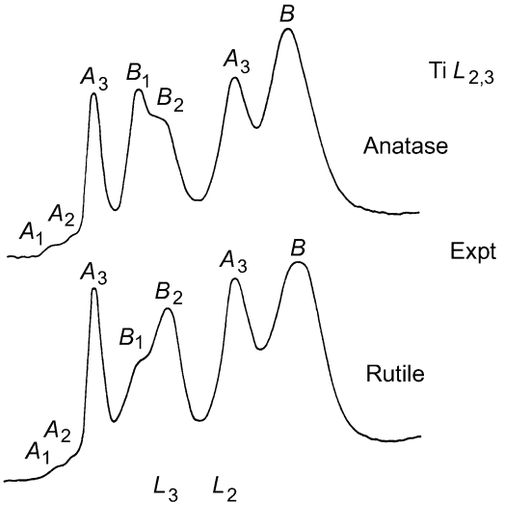

Fig. 4.3.4.27. High-energy resolution spectra on the $L_{2,3}$ titanium edge from two phases (rutile and anatase) of TiO_2. Each atomic line L_3 and L_2 is split into two components A and B by crystal-field effects. The new level of splitting B_1B_2 that distinguishes the two spectra is not yet understood. In Ti metal, the L_3 and L_2 lines are not split by structural effects [courtesy of Brydson *et al.* (1989)].

Wilkins, 1982). Core-loss spectroscopy, however, imposes specific conditions on the accessible final state: the overlap with the initial core wavefunction involves a projection in space on the site of the core hole, and the dominant dipole selection rules are responsible for angular symmetry selection. When extending the band-structure calculations to energy states rather high above the Fermi level, more elaborate methods, combining the conceptual advantage of the tight-binding method with the accuracy of *ab initio* pseudopotential calculations, have been developed (Janssen & Sankey, 1987). This self-consistent pseudo-atomic orbital band calculation has been used to describe ELNES structures on different covalent solids (Weng, Rez & Ma, 1989; Weng, Rez & Sankey, 1989).

The most promising description at present is the multiple scattering method developed for X-ray absorption spectra by Durham, Pendry & Hodges (1981) and Vvedensky, Saldin & Pendry (1985). It interprets the spectral modulations, in the energy range 10 to 30 eV above the edge, as due to interference effects, on the excited site, between all waves back-scattered by the neighbouring atoms (see Fig. 4.3.4.29). This multiple scattering description in real space should in principle converge towards the local point of view in the solid-state band model, calculated in reciprocal space (Heine, 1980). As an example investigated by EELS, the oxygen and magnesium *K* edges in MgO have been calculated by Lindner, Sauer, Engel & Kambe (1986) and by Weng & Rez (1989) for increased numbers of coordination shells and different potential models (representing variable ionicities). Fig. 4.3.4.30 shows the comparison of an experimental spectrum with such a calculation. Another useful idea emerging from this model is the simple relation, expressed by Bianconi, Fritsch, Calas & Petiau (1985):

$$(E_r - E_b)\, d^2 = C, \qquad (4.3.4.48)$$

where E_r is the energy position of a given resonance peak attributed to multiple scattering from a given shell of neighbours (d is the distance to this shell), and E_b is a reference energy close to the threshold energy. This simple law, advertised as the way of measuring 'bond lengths with a ruler' (Stohr, Sette & Jonson, 1984), seems to be quite useful when comparing similar structures (Lytle, Greegor & Panson, 1988).

Other effects, generally described as multi-electron contributions, cannot be systematically omitted. They all deal with the presence of a core hole on the excited atom and with its influence on the distribution of accessible electron states. Of particular importance are the intra-atomic configuration interactions for white lines, as explained by Zaanen, Sawatsky, Fink, Speier & Fuggle (1985) for L_3 and L_2 lines in transition metals and by Thole, van der Laan, Fuggle, Swatsky, Karnatak & Esteva (1985) for $M_{4,5}$ lines in rare-earth elements.

(*c*) *The extended fine structures* (EXELFS) are equivalent to the well known EXAFS oscillations in X-ray absorption spectroscopy (Sayers, Stern & Lytle, 1971; Teo & Joy, 1981). Within the previously described multiscattering theory, it corresponds to the first step, the single scattering regime (see Fig. 4.3.4.29*a*). These extended oscillations are due to the interference on the excited atom between the outgoing excited

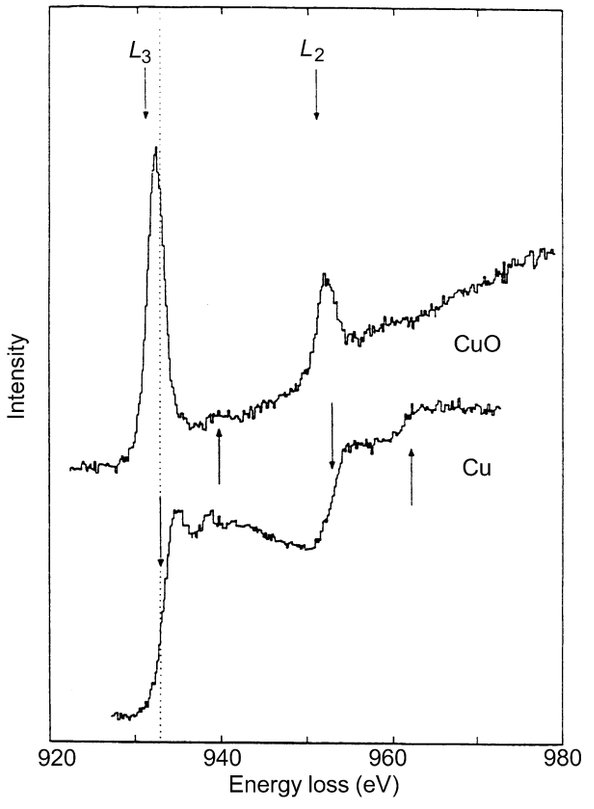

Fig. 4.3.4.28. The dramatic change in near-edge fine structures on the L_3 and L_2 lines of Cu, from Cu metal to CuO. The appearance of the intense narrow white lines is due to the existence of vacant *d* states close to the Fermi level [courtesy of Leapman *et al*. (1982)].

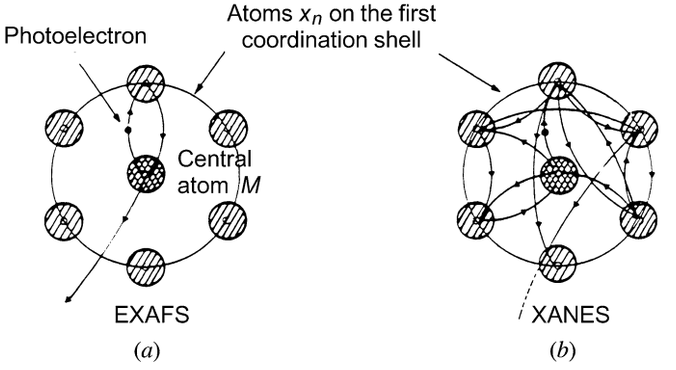

Fig. 4.3.4.29. Illustration of the single and multiple scattering effects used to describe the final wavefunction on the excited site. This theory is very fruitful for understanding and interpreting EXELFS and ELNES features, respectively equivalent to EXAFS and XANES encountered in X-ray absorption spectra.

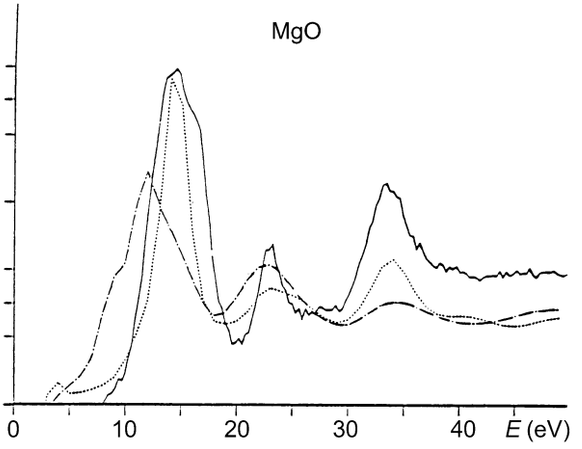

Fig. 4.3.4.30. Comparison of the experimental O *K* edge (solid line) with calculated profiles in the multiple scattering approach [courtesy of Weng & Rez (1989)].

electron wavefunction and its components reflected on the nearest-neighbour atoms. This interference is destructive or constructive depending on the ratio between the return path length $2r_i$ (where r_i is the radial distance with the ith shell of backscattering atoms) and the wavelength of the excited electron. Fourier analysis of EXELFS structures, from 50 eV above the ionization threshold, gives the radial distribution function around this specific site. This is mostly a technique for measuring the local short-range order. Its accuracy has been established to be better than 0.1 Å on nearest-neighbour distances with test specimens, but such performance requires correction procedures for phase shifts. The method therefore seems more promising for measuring changes in interatomic distances in specimens of the same chemical composition. The major advantage of EXELFS is its applicability for small specimen volumes that can moreover be characterized by other high-resolution electron-microscopy modes. It is also possible to investigate bond lengths in different directions by selecting the scattering angle of the transmitted electron and the specimen orientation (Disko, Krivanek & Rez, 1982). On the other hand, the major limitations of EXELFS are due to the dose requirements for sufficient SNR and to the fact that the accessible excitation range is limited to edges below ~2–3 keV and to oscillation domains ~200 or 300 eV at the maximum.

4.3.4.4.4. *Applications for core-loss spectroscopy*

(*a*) *Quantitative microanalysis*

The main field of application of core-loss EELS spectroscopy has been its use for local chemical analysis (Maher, 1979; Colliex, 1984; Egerton, 1986). The occurrence of an edge superimposed on the regularly decreasing background of an EELS spectrum is an indication of the presence of the associated element within the analysed volume.

Methods have been developed to extract quantitative composition information from these spectra. The basic idea lies in the linear relationship between the measured signal (S) and the number (N) of atoms responsible for it (this is valid in the single core-loss domain for specimen thickness, *i.e.* up to several micrometres):

$$S = I_0 N \sigma, \tag{4.3.4.49}$$

where I_0 is the incident-beam intensity and σ the relevant excitation cross section in the experimental conditions used, and N is the number of atoms per unit area of specimen. As a satisfactory approximation for taking into account multiple scattering events (either elastic or inelastic in the low-loss region), Egerton (1978) has proposed that equation (4.3.4.49) be rewritten:

$$S(\beta, \Delta) = I_0(\beta, \Delta) N \sigma(\beta, \Delta), \tag{4.3.4.50}$$

where all quantities correspond to a limited angle of collection β and to a limited integration window Δ (eV) above threshold for signal measurement.

A major problem is the evaluation of the signal itself after background subtraction. The method generally used, demonstrated in Fig. 4.3.4.31, involves extrapolating a modelized background profile below the core loss of interest. Following Egerton (1978), the choice of a power law $B(\Delta E) = A \Delta E^{-R}$ is satisfactory in many cases, and the signal is then defined as

$$S(\Delta) = \int_{E_c}^{E_c+\Delta} [I(\Delta E) - B(\Delta E)] \, \mathrm{d}(\Delta E). \tag{4.3.4.51}$$

Numerical methods have been developed to perform this process with a well controlled analysis of statistical errors (Trebbia, 1988).

In many cases, one is interested in elemental ratios; consequently, the useful formula becomes

$$\frac{N_A}{N_B} = \frac{S_A(\beta, \Delta)}{S_B(\beta, \Delta)} \frac{\sigma_B(\beta, \Delta)}{\sigma_A(\beta, \Delta)}. \tag{4.3.4.52}$$

This can be used to determine the N_A/N_B ratio without standards, if the cross-section ratio σ_B/σ_A (also called the k_{AB} factor) is previously known: accuracy at present is limited to ±5% for most edges. But it is also possible to extract from this formula the cross-section (or k factor) experimental values for comparison with the calculated ones, if the local stoichiometry of the specimen is satisfactorily known [Hofer, Golob & Brunegger (1988) and Manoubi *et al.* (1989) for the $M_{4,5}$ edges].

Improvements have recently been made in order to reduce the different sources of errors. For medium-thickness specimens (*i.e.* for $t \simeq \lambda_p$ where λ_P is the mean free path for plasmon excitation), deconvolution techniques are introduced for a safer determination of the signal. When the background extrapolation method cannot be used, *i.e.* when edges overlap noticeably, new approaches (such as illustrated in Fig. 4.3.4.25) try to determine the best simulated profile over the whole energy-loss range of interest. It requires several contributions, either deduced from previous measurements on standard (Shuman & Somlyo, 1987; Leapman & Swyt, 1988), or from reasonable mathematical models with different contributions for dealing with transitions towards bound states or continuum states (Manoubi, Tence, Walls & Colliex, 1990).

(*b*) *Detection limits*

This method has been shown to be the most successful of all EM techniques in terms of ultimate mass sensitivity and associated spatial resolution. This is due to the strong probability of excitation for the signals of interest (primary ionization event) and to the good localization of the characteristic even within the irradiated volume of material. Variations in composition have been recorded at a subnanometre level (Scheinfein & Isaacson, 1986; Colliex, 1985; Colliex, Maurice & Ugarte, 1989). In terms of ultimate sensitivity (minimum number of identified atoms), the range of a few tens of atoms (~10^{-21} g) has been reached as early as about 15 years ago in the pioneering work of

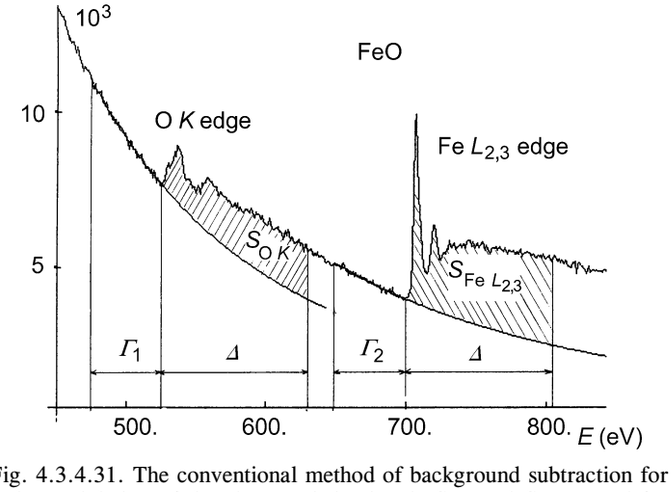

Fig. 4.3.4.31. The conventional method of background subtraction for the evalulation of the characteristic signals S_{OK} and $S_{Fe L_{2,3}}$ used for quantitative elemental analysis (to be compared with the approach described in Fig. 4.3.4.25).

Isaacson & Johnson (1975). Very recently, a level close to the single-atom identification has been demonstrated (Mory & Colliex, 1989). A major obstacle is then often radiation damage, and consequent specimen modification induced by the very intense primary dose required for obtaining sufficient SNR values.

On the other hand, the EELS technique has long been less fruitful for investigating low concentrations of impurities within a matrix. This is a consequence of the very high intrinsic background under the edges of interest: in most applications, the atomic concentration detection limit was in the range 10^{-3} to 10^{-2}. The introduction of satisfactory methods for processing the systematic sources of noise in spectra acquired with parallel detection devices (Shuman & Kruit, 1985) has greatly modified this situation. One can now take full benefit from the very high number of counts thus recorded within a reasonable time (10^6 to 10^7 counts per channel) and detection of calcium of the order of 10^{-5} atomic concentration in an organic matrix has been demonstrated by Shuman & Somlyo (1987).

(*c*) *Crystallographic information in EELS*

Although not particularly suited to solving crystal-structure problems, EELS carries structural information at different levels:

In a crystalline specimen, one detects orientation effects on the intensity of core-loss edges. This is a consequence of the channelling of the Bloch standing waves as a function of the crystal orientation This observation requires well collimated angular conditions and inelastic localization better than the lattice spacing responsible for elastic diffraction. When these criteria apply, the changes in core-loss excitations with crystallographic orientation can be used to determine the crystallographic site of specific atoms (Tafto & Krivanek, 1982). An equivalent method, known as ALCHEMI (atom location by channelling enhanced microanalysis), which involves measuring the change of X-ray production as a function of crystal orientation, has been applied to the determination of the preferential site for substitutional impurities in many crystals (Spence & Tafto, 1983).

Energy-filtered electron-diffraction patterns of core-loss edges could reveal the symmetry of the local coordination of selected atomic species rather than the symmetry of the crystal as a whole. This type of information should be compared with ELNES data (Spence, 1981).

At large scattering angles, and for energy losses far beyond the excitation threshold, the Bethe ridge [or electron Compton profile (see §§4.3.4.3.3 and 4.3.4.4.2)] constitutes a major feature easily observable in energy-filtered diffraction patterns (Reimer & Rennekamp, 1989). The width of this feature is associated with the momentum distribution of the excited electrons (Williams & Bourdillon, 1982). Quantitative analysis of the data is similar to the Fourier method for EXELFS oscillations. After subtracting the background contribution, the spectrum is converted into momentum space and Fourier transformed to obtain the reciprocal form factor $B(r)$: it is the autocorrelation of the ground-state wavefunction in a direction specified by the scattering vector $\mathbf{q}$. This technique of data analysis to study electron momentum densities is directly developed from high-energy photon-scattering experiments (Williams, Sparrow & Egerton, 1984).

4.3.4.5. *Conclusions*

Since the early work of Hillier & Baker (1944), EELS spectroscopy has established itself as a prominent technique for investigating various aspects of the electronic structure of solids, As a fundamental application, it is now possible to construct a self-consistent set of data for a substance by combination of optical or energy-loss functions over a wide spectral range (Altarelli & Smith, 1974; Shiles, Sazaki, Inokuti & Smith, 1980: Hagemann, Gudat & Kunz, 1975). Sum-rule tests provide useful guidance in selecting the best values from the available measurements. The Thomas–Reiche–Kuhn *f*-sum rule can be expressed in a number of equivalent forms, which all require the knowledge of a function $[\varepsilon_2, \kappa, \mathrm{Im}(-1/\varepsilon)]$ describing dissipative processes over all frequencies:

$$\left.\begin{aligned} \int_0^\infty \omega\varepsilon_2(\omega)\,\mathrm{d}\omega &= \frac{\pi}{2}\omega_p^2, \\ \int_0^\infty \omega\kappa(\omega)\,\mathrm{d}\omega &= \frac{\pi}{4}\omega_p^2, \\ \int_0^\infty \omega\left(-\frac{1}{\varepsilon(\omega)}\right)\mathrm{d}\omega &= \frac{\pi}{2}\omega_p^2. \end{aligned}\right\} \tag{4.3.4.53}$$

One defines the effective number density n_{eff} of electrons contributing to these various absorption processes at an energy $\hbar\omega$ by the partial *f* sums:

$$\left.\begin{aligned} n_{\mathrm{eff}}(\omega)|_{\varepsilon_2} &= \frac{m_0}{2\pi^2 e^2}\int_0^\omega \omega'\varepsilon_2(\omega')\,\mathrm{d}\omega', \\ n_{\mathrm{eff}}(\omega)|_{\kappa} &= \frac{m_0}{\pi^2 e^2}\int_0^\omega \omega'\kappa(\omega')\,\mathrm{d}\omega', \\ n_{\mathrm{eff}}(\omega)|_{-1/\varepsilon} &= \frac{m_0}{2\pi^2 e^2}\int_0^\omega \omega'\left[-\frac{1}{\varepsilon(\omega')}\right]\mathrm{d}\omega'. \end{aligned}\right\} \tag{4.3.4.54}$$

As an example, the values of $n_{\mathrm{eff}}(\omega)$ from the infrared to beyond the *K*-shell excitation energy for metallic aluminium are shown in Fig. 4.3.4.32. In this case, the conduction and core-electron contributions are well separated. One sees that the excitation of conduction electrons is virtually completed above the plasmon resonance only, but the different behaviour of the integrands below this value is a consequence of the fact that they describe different properties of matter: $\varepsilon_2(\omega)$ is a measure of the rate of energy dissipation from an electromagnetic wave, $\kappa(\omega)$ describes

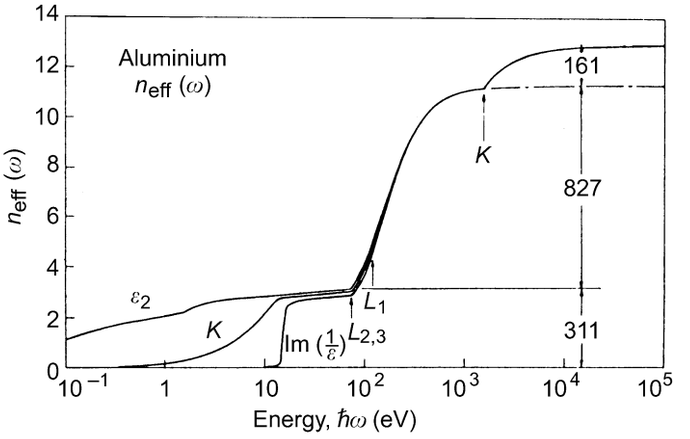

Fig. 4.3.4.32. Values of n_{eff} for metallic aluminium based on composite optical data [courtesy of Shiles *et al.* (1980)].

the decrease in amplitude of the wave, and $\mathrm{Im}[-\varepsilon^{-1}(\omega)]$ is related to the energy loss of a fast electron. The above curve shows some exchange of oscillator strength from core to valence electrons, arising from the Pauli principle, which forbids transitions to occupied states for the deeper electrons.

More practically, in the microanalytical domain, the combination of high performance attained by using EELS with parallel detection (*i.e.* energy resolution below 1 eV, spatial resolution below 1 nm, minimum concentration below 10^{-3} atom, time resolution below 10 ms) makes it a unique tool for studying local electronic properties in solid specimens.

4.3.5. Oriented texture patterns (By B. B. Zvyagin)

4.3.5.1. *Texture patterns*

The formation of textures in specimens for diffraction experiments is a natural consequence of the tendency for crystals of a highly anisotropic shape to deposit with a preferred orientation. The corresponding diffraction patterns may present some special advantages for the solution of problems of phase and structure analysis. Lamellar textures composed of crystals with the most fully developed face parallel to a plane but randomly rotated about its normal are specially important. The ease of interpretation of patterns of such textures when oriented obliquely to the primary beam (*OT* patterns) is a valuable property of the electron-diffraction method (Pinsker, 1953; Vainshtein, 1964; Zvyagin, 1967; Zvyagin, Vrublevskaya, Zhukhlistov, Sidorenko, Soboleva & Fedotov, 1979). Texture patterns (*T* patterns) are also useful in X-ray diffraction (Krinary, 1975; Mamy & Gaultier, 1976; Plançon, Rousseaux, Tchoubar, Tchoubar, Krinari & Drits, 1982).

4.3.5.2. *Lattice plane oriented perpendicular to a direction (lamellar texture)*

If in the plane of orientation (the texture basis) the crystal has a two-dimensional cell a, b, γ, the c^* axis of the reciprocal cell will be the texture axis. Reciprocal-lattice rods parallel to c^* intersect the plane normal to them (the ab plane of the direct lattice) in the positions hk of a two-dimensional net that has periods $1/a\sin\gamma$ and $1/b\sin\gamma$ with an angle $\gamma' = \pi - \gamma$ between them, whatever the direction of the c axis in the direct lattice.

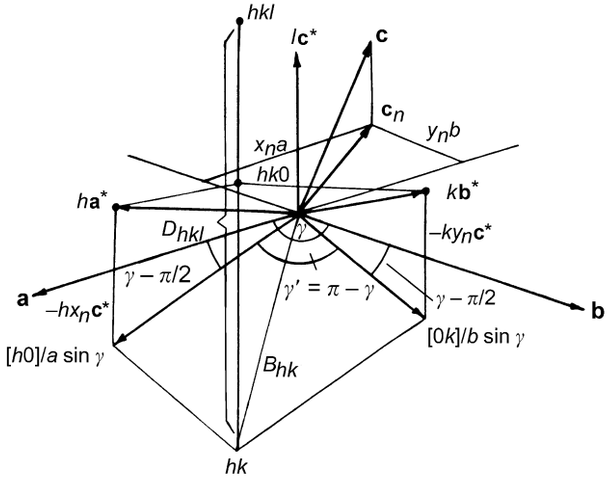

Fig. 4.3.5.1. The relative orientations of the direct and the reciprocal axes and their projections on the plane ab, with indication of the distances B_{hk} and D_{hkl} that define the positions of reflections in lamellar texture patterns.

The latter is defined by the absolute value c and the normal projection c_n on the ab plane, with components x_n, y_n along the axes a, b. In the triclinic case,

$$x_n = (c/a)(\cos\beta - \cos\alpha\cos\gamma)/\sin^2\gamma \qquad (4.3.5.1)$$

$$y_n = (c/b)(\cos\alpha - \cos\beta\cos\gamma)/\sin^2\gamma \qquad (4.3.5.2)$$

(Zvyagin *et al.*, 1979). The lattice points of each rod with constant hk and integer l are at intervals of $c^* = 1/d_{001}$, but their real positions, described by their distances D_{hkl} from the plane ab, depend on the projections of the axes a^* and b^* on c^* (see Fig. 4.3.5.1), the equations

$$x_n = -a^*\cos\beta^*/c^* \qquad (4.3.5.3)$$

$$y_n = -b^*\cos\alpha^*/c^* \qquad (4.3.5.4)$$

being satisfied.

The reciprocal-space representation of a lamellar texture is formed by the rotation of the reciprocal lattice of a single crystal about the c^* axis. The rods hk become cylinders and the lattice points become circles lying on the cylinders. In the case of high-energy electron diffraction (HEED), the wavelength of the electrons is very short, and the Ewald sphere, of radius $1/\lambda$, is so great that it may be approximated by a plane passing through the origin of reciprocal space and normal to the incident beam. The patterns differ in their geometry, depending on the angle φ through which the specimen is tilted from perpendicularity to the primary beam. At $\varphi = 0$, the pattern consists of hk rings. When $\varphi \neq 0$ it contains a two-dimensional set of reflections hkl falling on hk ellipses formed by oblique sections of the hk cylinders. In the limiting case of $\varphi = \pi/2$, the ellipses degenerate into pairs of parallel straight lines theoretically containing the maximum numbers of reflections. The reflection positions are defined by two kinds of distances: (1) between the straight lines hk (length of the short axes of the ellipses hk):

$$B_{hk} = (1/\sin\gamma)(h^2/a^2 + k^2/b^2 - 2hk\cos\gamma/ab)^{1/2} \qquad (4.3.5.5)$$

and (2) from the reflection hkl to the line of the short axes:

$$D_{hkl} = (ha^*\cos\beta^*/c^* + kb^*\cos\alpha^*/c^* + l)c^* \qquad (4.3.5.6)$$

$$= (-hx_n - ky_n + l)/d_{001}. \qquad (4.3.5.7)$$

In patterns obtained under real conditions ($0 < \varphi < \pi/2$, accelerating voltage V proportional to λ^{-2}, distance L between the specimen and the screen), these values are presented in the scale of $L\lambda$, D_{hkl} also being proportional to $1/\sin\varphi$ with maximum value $D_{\max} = B_{hk}\tan\varphi$ for the registrable reflections. The values of B_{hk} and D_{hkl}, determined by the unit cells and the indices hkl, are the objects of the geometrical analysis of the *OT* patterns. When the symmetry is higher than triclinic, the expression for B_{hk} and D_{hkl} are much simpler.

Such *OT* patterns are very informative, because the regular two-dimensional distribution of the hkl reflections permits definite indexing, cell determination, and intensity measurements. For low-symmetry and fine-grained substances, they present unique advantages for phase identification, polytypism studies, and structure analysis.

In the X-ray study of textures, it is impossible to neglect the curvature of the Ewald sphere and the number of reflections recorded is restricted to larger d values. However, there are advantages in that thicker specimens can be used and reflections with small values of B_{hk}, especially the $00l$ reflections, can be recorded. Such patterns are obtained in usual powder cameras with the incident beam parallel to the platelets of the oriented aggregate and are recorded on photographic film in the form of hkl reflection sequences along hk lines, as was demonstrated by

references